nature neuroscience

Article

https://doi.org/10.1038/s41593-023-01494-2

TFEB–vacuolar ATPase signaling regulates lysosomal function and microglial activation in tauopathy

Received: 5 February 2023

Accepted: 13 October 2023

Published online: 20 November 2023

Check for updates

Baiping Wang[1,2,9], Heidi Martini-Stoica[1,3,6,9], Chuangye Qi[1,9], Tzu-Chiao Lu[1], Shuo Wang[1], Wen Xiong[1], Yanyan Qi[1], Yin Xu[1,7], Marco Sardiello[2,4,8], Hongjie Li[1,2] & Hui Zheng[1,2,5]

Transcription factor EB (TFEB) mediates gene expression through binding to the coordinated lysosome expression and regulation (CLEAR) sequence. TFEB targets include subunits of the vacuolar ATPase (v-ATPase), which are essential for lysosome acidification. Single-nucleus RNA sequencing of wild-type and PS19 (Tau) transgenic mice expressing the P301S mutant tau identified three unique microglia subclusters in Tau mice that were associated with heightened lysosome and immune pathway genes. To explore the lysosome–immune relationship, we specifically disrupted the TFEB–v-ATPase signaling by creating a knock-in mouse line in which the CLEAR sequence of one of the v-ATPase subunits, *Atp6v1h*, was mutated. CLEAR mutant exhibited a muted response to TFEB, resulting in impaired lysosomal acidification and activity. Crossing the CLEAR mutant with Tau mice led to higher tau pathology but diminished microglia response. These microglia were enriched in a subcluster low in mTOR and HIF-1 pathways and were locked in a homeostatic state. Our studies demonstrate a physiological function of TFEB–v-ATPase signaling in maintaining lysosomal homeostasis and a critical role of the lysosome in mounting a microglia and immune response in tauopathy and Alzheimer's disease.

Lysosomes are intracellular organelles essential for the degradation of protein aggregates and other macromolecules and organelles. Whereas intracellular materials are presented to the lysosome via autophagy, extracellular cargos are taken up through endocytosis or phagocytosis and delivered to the lysosome for clearance. Traditionally regarded as a static organelle for terminal degradation, emerging evidence demonstrates that lysosomes are highly dynamic and tightly regulated[1]. Impaired lysosomal homeostasis has been implicated in aging and age-associated neurodegenerative diseases including Alzheimer's disease (AD), Parkinson's disease and frontotemporal degeneration[2].

The transcription factor EB (TFEB) plays a central role in lysosome regulation and signaling[3]. It responds to lysosomal pH and content through the lysosome nutrient sensing (LYNUS) machinery composed of vacuolar ATPase (v-ATPase), Rag-GTPases and Ragulator, and the recruitment of mTORC1, to undergo cytoplasmic to nucleus trafficking. Inside the nucleus, TFEB promotes the transcription of its target genes

[1]Huffington Center on Aging, Baylor College of Medicine, Houston, TX, USA. [2]Department of Molecular and Human Genetics, Baylor College of Medicine, Houston, TX, USA. [3]Medical Scientist Training Program, Baylor College of Medicine, Houston, TX, USA. [4]Dan and Jan Duncan Neurological Research Institute, Baylor College of Medicine, Houston, TX, USA. [5]Department of Neuroscience, Baylor College of Medicine, Houston, TX, USA. [6]Present address: Department of Otolaryngology, University of North Carolina School of Medicine, Chapel Hill, NC, USA. [7]Present address: School of Mental Health and Psychological Sciences, Anhui Medical University, Anhui, China. [8]Present address: Department of Pediatrics, Washington University School of Medicine, St Louis, MO, USA. [9]These authors contributed equally: Baiping Wang, Heidi Martini-Stoica, Chuangye Qi. e-mail: huiz@bcm.edu

through binding to the coordinated lysosomal expression and regulation (CLEAR) motifs[4,5], the network of which consists of genes involved in autophagy, lysosomal biogenesis, lysosomal exocytosis and endocytosis[6]. Thus, TFEB is known as a master regulator of the autophagy and lysosomal pathway. Accordingly, we and others have reported that TFEB overexpression led to the suppression of Aβ and tau pathologies characteristic of AD and other tauopathy diseases in mice[7–12]. Whereas the beneficial effects of exogenous TFEB expression in disease models are abundantly documented, the role of endogenous TFEB in AD pathogenesis is less well defined. Further, whether these effects are solely mediated through lysosomal clearance remains unclear.

A key determinant of the lysosomal functionality is its acidic pH controlled by v-ATPase[13]. Reduced v-ATPase activity and defective lysosomal acidification have been implicated as early events in AD progression[2]. In addition to promoting the expression of a broad range of lysosomal enzymes, TFEB targets also include subunits of the v-ATPase[6]. Of interest, the *Drosophila* TFEB homolog Mitf has been shown to control the expression of all v-ATPase subunit genes[14,15], indicating evolutionary conservation of the TFEB–v-ATPase regulatory pathway. We found that the v-ATPase and lysosomal pathway as well as the immune pathway genes were prominently upregulated in the brains of PS19 transgenic mice expressing the P301S mutant tau (hereafter referred to as Tau). Through manipulating the endogenous TFEB–v-ATPase signaling, executed by mutagenesis of the CLEAR sequence in the promoter of one of the v-ATPase subunits, *Atp6v1h*, we demonstrate that specific disruption of the TFEB-dependent *Atp6v1h* transcriptional regulation leads to impaired v-ATPase activity and lysosomal function under physiological conditions. Intriguingly, microglia with the disrupted TFEB–v-ATPase signaling fail to be activated in Tau mice, revealing an essential role of the lysosome in initiating microglia and immune pathway activation.

Results

Upregulated TFEB and lysosomal pathway in tauopathy

Our previous work revealed that TFEB and several of its lysosomal target genes were significantly increased in human tauopathy brain samples and in Tau mice[12]. To investigate this phenomenon further, we conducted hippocampal bulk RNA sequencing in wild-type (WT) and Tau mice either before (4 months) or after (9 months) the development of tangle-like pathologies (Supplementary Table 1). We found only a few differentially expressed genes (DEGs) between WT and Tau mice at 4 months of age. In contrast, we identified 825 significantly upregulated genes and 89 significantly downregulated genes (cutoff of false discovery rate (FDR) < 0.05 and fold change > 1.5) in 9-month-old Tau mice compared to WT (Extended Data Fig. 1a–d). These were validated by quantitative polymerase chain reaction (qPCR) analysis (Extended Data Fig. 1e,f). These results indicate that the DEGs identified in 9-month-old Tau mouse brains were the consequences of mutant tau aggregates associated with aging rather than transgene overexpression. Gene set enrichment analysis (GSEA) revealed highly significant enrichment of both the lysosome and inflammatory response pathway genes in Tau mice (Fig. 1a,b).

To directly test whether the mutant tau aggregates induce TFEB activation and lysosomal gene expression, we first examined endogenous TFEB localization in HEK293 cells in response to intracellular mutant tau expression or with addition of tau preformed fibrils (Pff), which converts soluble mutant tau to insoluble aggregates[16]. When the cells were fed with normal serum-containing medium, TFEB was predominantly expressed in the cytoplasm, but translocated to the nucleus when the cells were serum starved or treated with bafilomycin, a v-ATPase inhibitor that induces lysosomal stress (Fig. 1c,d). We transfected either the empty vector or the P301L mutant tau to HEK293 cells, and a portion of the Tau cells were seeded with Pff. Immunostaining for endogenous TFEB showed that, compared to vector transfected controls, the Tau-expressing cells showed a trend of higher percentage of nuclear TFEB ($P = 0.086$), and this became significant when the Tau-expressing cells were seeded with Pff (Tau + Pff) (Fig. 1c,d), indicating that tau aggregation induces or at least occurs in a temporally linked fashion to TFEB nuclear translocation. This was further validated by cotransfecting TFEB-green fluorescent protein (GFP) with empty vector or P301L tau to HEK293 cells, followed by treating the cells with either the vehicle (PBS) or tau Pff. Immunostaining with the tau confirmation antibody MC1 (Fig. 1e) followed by quantification (Fig. 1f) showed that, as expected, the MC1-positive cells can only be detected in the Tau + Pff group, and these cells displayed significantly higher nuclear TFEB compared to other conditions. These results support a model whereby seeding-induced insoluble mutant tau triggers TFEB nuclear translocation and downstream lysosomal gene expression (Fig. 1g).

snRNA-seq revealed altered microglial profiles in Tau mice

Having established upregulated lysosomal and immune pathways in bulk brains of Tau mice, we next sought to understand the cell types contributing to the changes by conducting single-nucleus RNA sequencing (snRNA-seq) of the hippocampus collected from 9-month-old WT and Tau mice. Nuclei isolated by fluorescence-activated cell sorting were profiled using the droplet-based 10x Genomics platform. After stringent quality control including doublet removal, batch effect correction and normalization (Extended Data Fig. 2a), we obtained a total of 55,254 high-quality single-cell transcriptomes (Supplementary Table 2), which were annotated into eight major cell types based on the expression of well-known cell-type-specific markers (Fig. 2a–c). Cell-type composition analysis between WT and Tau mice revealed that certain neuronal populations, particularly granule cell cluster, were strongly reduced in Tau mice, indicating neurodegeneration (Fig. 2b). By contrast, the microglia population was greatly expanded in Tau mice. Further analysis identified 915 DEGs in the microglia of Tau mice compared with WT mice, of which 600 were significantly upregulated genes with a cutoff of FDR < 0.05 and $\log_2$(fold change) > 0.25. We found that signatures of disease-associated microglia (DAM) and microglia of neurodegeneration type (MGnD)[17,18] were among the top upregulated DEGs (Fig. 2d). Gene Ontology (GO) pathway analysis of the upregulated genes revealed immune and lysosome pathways as top enriched pathways in Tau microglia (Fig. 2e).

Fig. 1 | Elevated TFEB and lysosomal pathway in PS19 (Tau) mice and by insoluble tau. a,**b**, GSEA of lysosome (**a**) and inflammatory (**b**) pathways in Tau mice ($n = 4$) compared with WT mice ($n = 5$) at 9 months. The statistical significance (nominal P value) of the normalized enrichment score (NES) was generated by employing an empirical phenotype-based permutation test procedure. **c**, Representative fluorescence images of HEK293 cells transfected with empty vector (Ctrl) or Tau-P301L expression vector (Tau), or Tau-expressing cells treated with Pff (Tau + Pff) and immune-stained with an anti-TFEB antibody for endogenous human TFEB (red) and DAPI (blue). Cells under normal growth (Fed) condition were used as a negative control whereas cells grown in serum-free medium (Starve) or treated with 200 nM bafilomycin (Baf) were used as positive controls. **d**, Quantification of percent TFEB nuclear localization showing significantly higher nuclear TFEB in the Tau + Pff group. $n = 13$ images/condition. One-way ANOVA with Sidak's correction. **e**, Representative fluorescence images of HEK293 cells cotransfected with TFEB-GFP plus empty vector (Ctrl) or Tau-P301L construct and treated with PBS or Pff, followed by staining with the MC1 antibody, showing prominent nuclear TFEB in MC1-positive cells. **f**, Quantification of TFEB-GFP nuclear/cytoplasmic ratio, showing significantly higher nuclear TFEB in Tau + Pff cells. $n = 10$ images (PBS Ctrl); 13 (Pff Ctrl); 12 (PBS Tau) and 10 (Pff Tau). Two-tailed t-test. **g**, A working model whereby Tau Pff converts cellular Tau from soluble to insoluble form, which in turn induces TFEB nuclear translocation and upregulation of lysosomal gene expression. Scale bar, 10 μm. Data are presented as average ± s.e.m. The experiments were repeated three times with each in triplicate. See also Extended Data Fig. 1.

https://doi.org/10.1038/s41593-023-01494-2

Further analysis of the microglia population identified seven subclusters (0–6, Fig. 3a). Subcluster 0 was most highly represented in WT microglia (Fig. 3b), which has the characteristics of homeostatic microglia with higher expression of *P2ry12*, *Ccr5* and *Siglech* (Fig. 3c and Extended Data Fig. 2b). This subpopulation was drastically reduced, whereas subcluster 1 was greatly expanded in Tau microglia. In addition, the Tau microglia gained two unique populations: subclusters 2 and 3 (Fig. 3a,b). Subclusters 1 and 2 were enriched for DAM signatures, such as *Apoe*, *Axl* and *Csf1*, whereas subcluster 3 resembled interferon (IFN)-responsive microglia with highest

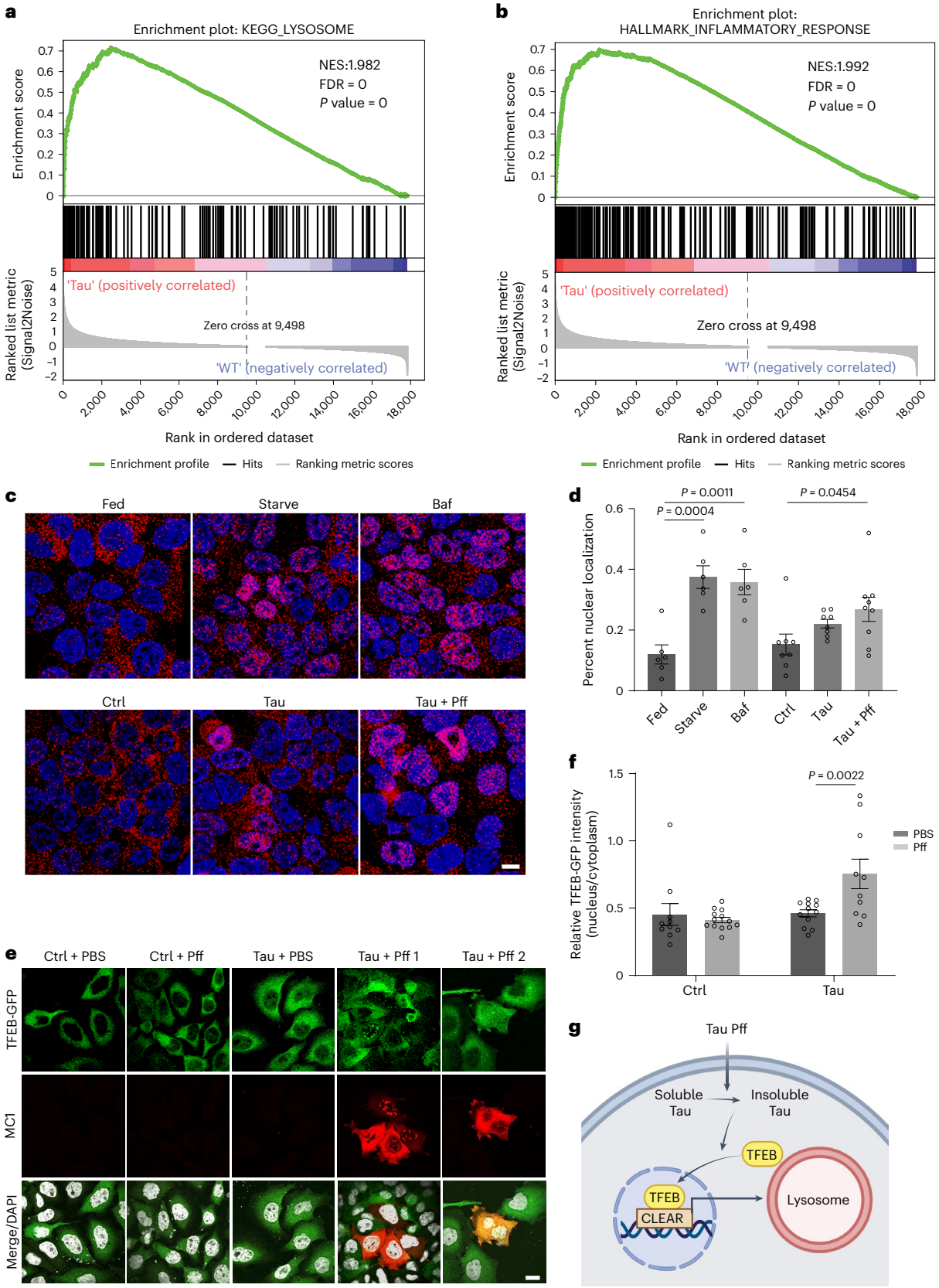

https://doi.org/10.1038/s41593-023-01494-2

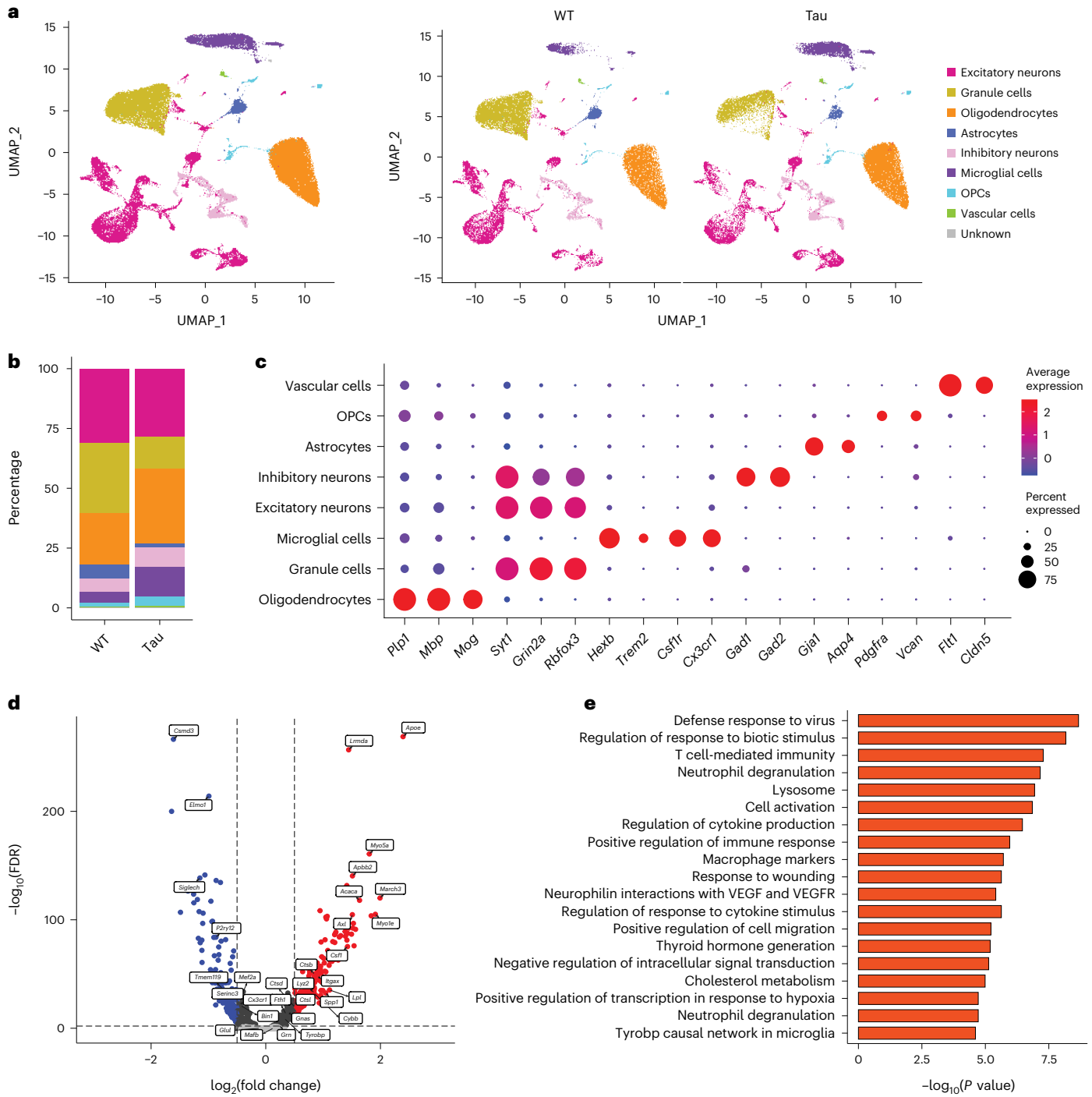

Fig. 2 | snRNA-seq revealed lysosome and immune pathway upregulation in microglia of Tau mice. a, Uniform Manifold Approximation and Projection (UMAP) representation of snRNA-seq analysis of 55,254 cells from hippocampus of WT and Tau mice (left panel) and across genotypes (right panel). Cell-type annotation was based on the expression of markers shown in **c**. **b**, Stacked barplot showing the cell-type compositions comparing Tau with WT. The bars are colored by their corresponding cell classes as labeled in **a**. **c**, Average scaled expression levels of selected signature genes for different cell types. **d**, Volcano plot showing DEGs for all microglia in Tau versus WT mice. Upregulated genes are highlighted in red; downregulated genes are highlighted in blue. **e**, GO enrichment analysis of biological processes for upregulated expressed genes in microglia of Tau versus WT mice. Hypergeometric test was used to identify significant enrichment pathways ($P < 0.01$). See also Extended Data Fig. 2.

expression of *Oasl2*, *Ifi204* and *Ifi207* (Fig. 3c and Extended Data Fig. 2b). Of note, we did not detect changes of *Trem2* in Tau microglia (Fig. 3e). Comparisons of upregulated DEGs between subclusters 1, 2 and 3 with 0 revealed that most of the subcluster 1 DEGs were included in subclusters 2 and 3, whereas subclusters 2 and 3 displayed distinct DEGs (Fig. 3d). Thus, subcluster 1 presents as an intermediate state, whereas subclusters 2 and 3 acquired distinct features. GO term enrichment analysis of upregulated genes between subcluster 2 and 0 revealed that lysosome and inflammatory response pathways were strongly overrepresented (Fig. 3e,f), whereas comparison between subcluster 3 and 0 identified antivirus- and IFN-responsive pathways as top enriched pathways, confirming subcluster 3 as

IFN-responsive microglia (Fig. 3g,h). Other smaller clusters were not further characterized.

TFEB regulates *Atp6v1h* expression through CLEAR sequences

The fact that the lysosomal pathway genes were prominently enriched in both the total microglia and subcluster 2 of Tau mice prompted us to seek further understanding of the functional implications of the lysosomal pathway and its relationship with the immune pathway. Although this could be achieved by TFEB manipulation, the many other nonlysosomal genes TFEB also targets, in particular the immune pathway genes[19], makes it difficult to delineate the lysosome-specific effect. We thus zoomed in on the TFEB lysosomal-specific target, the v-ATPase, given its key role in regulating lysosomal pH and activity. We found that most of the v-ATPase subunit genes were upregulated in Tau microglia (Fig. 4a), and hypothesized that disruption of TFEB–v-ATPase transcriptional regulation through mutagenizing the TFEB-binding CLEAR motif may lead to reduced v-ATPase activity and impaired lysosomal function. We chose *Atp6v1h* as it displays strong TFEB binding with two tandem repeat CLEAR sequences within its promoter region, whereas other subunit genes have one consensus sequence or exhibit weak TFEB binding (Fig. 4b, Extended Data Fig. 3). Chromatin immunoprecipitation (ChIP) of N2a cells transfected with GFP-FLAG or TFEB-FLAG using an anti-FLAG antibody followed by qPCR confirmed TFEB binding to the CLEAR sequence of the *Atp6v1h* promoter (Fig. 4c). *Mcoln1* was used as a positive control whereas Chr 1, 2 and 3 representing gene deserts of respective chromosomes lacking CLEAR sequences were used as negative controls. To validate that TFEB–CLEAR interaction promotes transcriptional activation, we cloned either the WT or the CLEAR mutant (CL) *Atp6v1h* promoter fragments to the firefly luciferase reporter, using the CLEAR-lacking AQP1-luciferase as a negative control, and cotransfected the constructs with either empty vector (CMV) or a TFEB expression vector. The luciferase assay showed that, compared with CMV controls, the WT *Atp6v1h* promoter responded to TFEB as expected, the TFEB response was blunted in the CL mutant as with the AQP1 control (Fig. 4d). Consistent with our earlier results that insoluble mutant tau induces TFEB activation (Fig. 1c–f), addition of Pff to HEK293 cells expressing P301L mutant tau (Tau + Pff) also induced the luciferase activity driven by the WT *Atp6v1h* promoter (Fig. 4e,f), and this effect was blocked when the CL mutant promoter was used (Fig. 4f). These data combined demonstrate that TFEB binds to the CLEAR sequence of the *Atp6v1h* promoter and activates its gene expression. Insoluble mutant tau induces TFEB nuclear translocation and enhances *Atp6v1h* transcription in a CLEAR-dependent manner.

Disruption of TFEB–ATP6V1H signaling impairs v-ATPase activity

To test the functional role of TFEB–ATP6V1H signaling in v-ATPase activity and lysosomal regulation in vivo, we introduced the same CLEAR mutation into the endogenous mouse *Atp6v1h* promoter via CRISPR–Cas9 technology. Mice homozygous for the CLEAR mutation (CL) showed a 25–30% reduction of the *Atp6v1h* transcript whereas neither TFEB nor other TFEB targets were affected (Fig. 4g). This is correlated with a mild reduction of ATP6V1H protein levels in whole brain extracts compared to wild-type controls, although this difference did not reach statistical significance (Fig. 4h). To directly validate that the CLEAR mutant obliterates TFEB's transcriptional regulation of *Atp6v1h*, we prepared primary mixed glia cultures from WT and CL homozygotes and treated them with Torin or starvation, which are known to induce TFEB nuclear localization and activation of its target genes[20–22]. In line with the bulk brain PCR, *Atp6v1h* transcripts were reduced by approximately 40% in CL homozygote cultures (Fig. 4i, Ctrl). In WT cultures, TFEB activation in both Torin- and starvation-treated conditions enhanced *Atp6v1h* transcription, whereas in CL cultures, the induction of *Atp6v1h* transcripts through these treatments was abolished (Fig. 4i). Collectively, these results reveal a physiological regulation of *Atp6v1h* transcription by TFEB through the CLEAR sequence and the specific disruption of TFEB–ATP6V1H signaling without affecting other TFEB targets in the CL mutant mice.

Next, we sought to determine whether the disrupted TFEB–ATP6V1H regulation leads to altered v-ATPase activity and lysosomal function. We first measured the lysosomal acidity in primary mixed glia cultures from WT and CL mice using Lysosensor Green DND-189, a pH-sensitive dye that exhibits increased fluorescence in acidic organelles. For positive controls, we treated WT cultures with bafilomycin or NH_4Cl which are known to elevate lysosomal pH. Compared with the WT control, the CL cultures showed significantly reduced Lysosensor fluorescence (Fig. 4j,k), indicating a defect in lysosomal acidification. To determine the functional consequences of reduced acidification in CL cultures, we utilized DQ-bovine serum albumin (DQ-BSA), which becomes fluorescent upon degradation, to assay the overall lysosomal hydrolase activity. Similar to Baf-treated WT controls, we showed that the intensity of DQ-BSA fluorescence was significantly decreased in CL cell cultures compared with WT cultures (Fig. 4l,m), indicating reduced lysosomal degradative capacity. Thus, disruption of TFEB–ATP6V1H signaling in the CLEAR mutant leads to impaired v-ATPase activity and defective lysosomal acidification and function.

The lysosomal phenotypes observed in the CL mutant could be attributed to reduced *Atp6v1h* expression or blunted TFEB–*Atp6v1h* transcriptional regulation. To differentiate these possibilities, we created *Atp6v1h* germline heterozygous knockout (VKO) mice. qPCR and Western blot analysis showed that both the *Atp6v1h* mRNA and ATP6V1H proteins levels were reduced by ~50% (Extended Data Fig. 4a,b). However, distinct from the CL mutant, measurement of lysosomal acidity using Lysosensor Green DND-189 and lysosomal hydrolytic activity by DQ-BSA fluorescence in WT and VKO primary mixed glia cultures revealed no genotype differences (Extended Data Fig. 4c–f). These results support an important role of TFEB–ATP6V1H signaling, not steady-state gene expression, in the control of v-ATPase and lysosomal activity.

Increased phospho-tau but reduced glial activation in Tau;CL mice

Having successfully created an in vivo model of lysosomal dysfunction, we next investigated the role of TFEB–v-ATPase regulation in tauopathy by crossing the CL mice with the Tau mice followed by analysis at 9 months of age. Western blotting of the forebrain hemispheres of Tau and Tau;CL mice showed a significant increase of phospho-tau species identified by PHF1 and CP13 antibodies in Tau;CL mice compared with Tau mice alone (Fig. 5a,b). These results were further confirmed by immunostaining of the brain slices with the AT8 antibody

Fig. 3 | Shift of microglia subclusters in Tau mice. a, UMAP representation of microglia subclusters (left panel) and the subclusters across genotypes (right panel). **b**, Stacked barplot showing the subcluster compositions of microglia comparing Tau with WT. The bars are colored by their corresponding cell classes as labeled in **a**. **c**, Violin plot showing the expression level of homeostatic microglia genes (*P2ry12*, *Ccr5* and *Siglech*), disease-associated microglia genes (*Apoe*, *Axl* and *Csf1*) and IFN-responsive microglia genes (*Oasl2*, *Ifi204* and *Ifi207*) in subclusters 0, 1, 2 and 3. **d**, Venn diagram summarizing the numbers of upregulated genes in subclusters 1, 2 and 3 versus 0. **e**, Volcano plot showing DEGs between subcluster 2 and subcluster 0. Upregulated genes are highlighted in red; downregulated genes are highlighted in blue. **f**, GO enrichment analysis of biological processes for upregulated expressed genes in subcluster 2 versus 0. **g**, Volcano plot showing DEGs for microglia subcluster 3 versus subcluster 0. Upregulated genes are highlighted in red; downregulated genes are highlighted in blue. **h**, GO enrichment analysis of biological processes for upregulated expressed genes in microglia of subcluster 3 versus 0. Hypergeometric test was used to identify significant enrichment pathways in **f** and **h** ($P < 0.01$).

https://doi.org/10.1038/s41593-023-01494-2

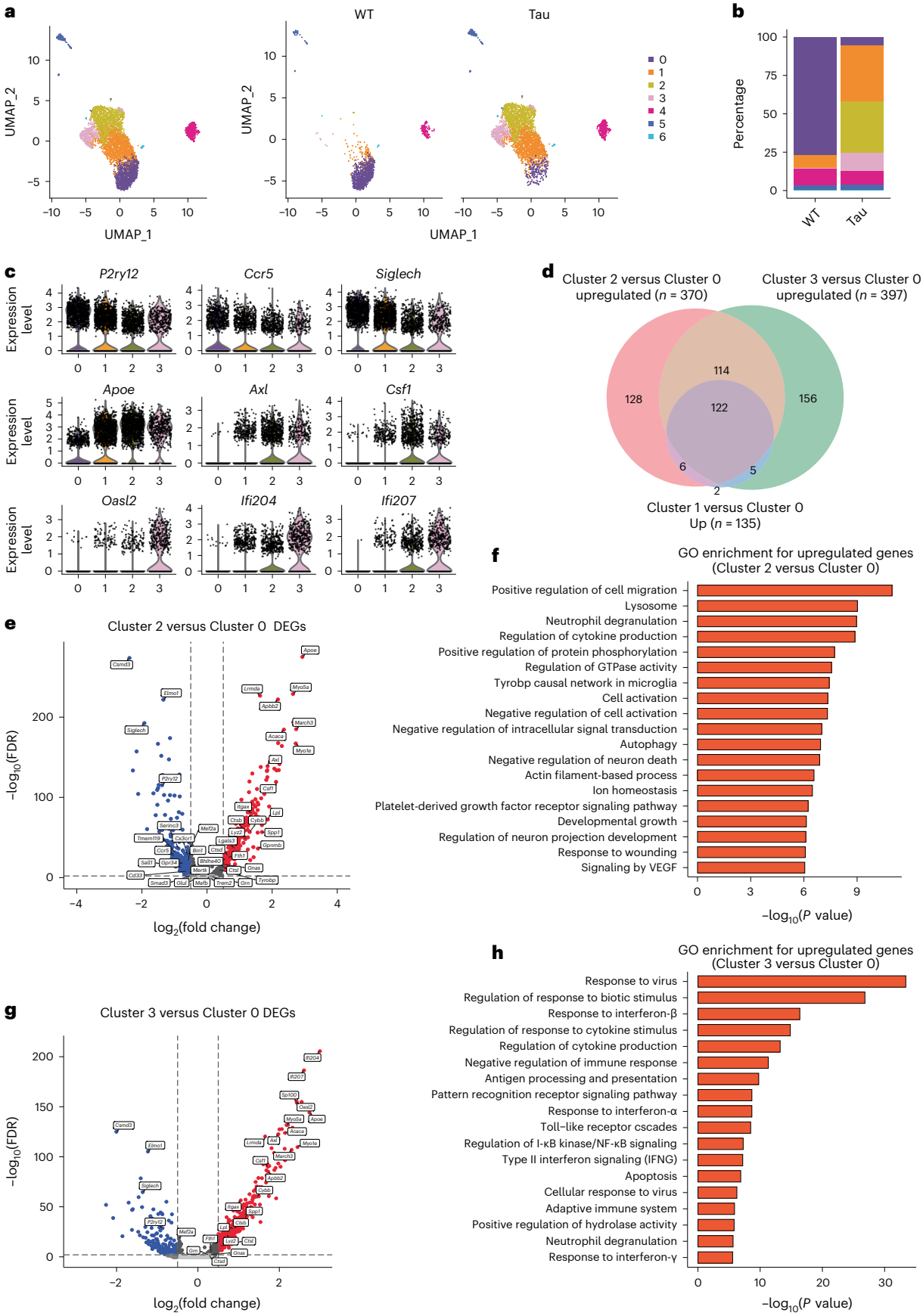

https://doi.org/10.1038/s41593-023-01494-2

(Fig. 5c,d). Surprisingly, coimmunostaining with anti-Iba1 and anti-CD68 antibodies, which are markers for general and phagocytic microglia, respectively, showed that, despite increased AT8-positive phospho-tau species, both the microglia numbers and Iba1 and CD68 immunofluorescence intensities were significantly lower in Tau;CL compared to littermate Tau controls (Fig. 5c and quantified in Fig. 5e–g). Further examination of microglia morphologies by 3D reconstruction and IMARIS quantification revealed that both the surface area and volume were reduced in Tau;CL compared with Tau alone (Fig. 5h–j), providing additional support for their dampened response to tauopathy. Immunostaining with an anti-GFAP antibody found similar reductions of GFAP-marked astrocytes in Tau mice expressing the CL mutation (Extended Data Fig. 5).

Consistent with normal lysosomal properties in the VKO mice, immunostaining using AT8 and anti-Iba1 and anti-GFAP antibodies revealed comparable levels of phospho-tau levels and glial immune intensities between Tau and Tau;VKO mice (Extended Data Fig. 6a–d). These were further validated by immunostaining with MC1, which recognizes misfolded tau species (Extended Data Fig. 6e,f), by Western blotting using total tau and phospho-tau (CP13 and PHF1) antibodies (Extended Data Fig. 6g,h) and by qPCR analysis of *Tnfa* and *Il1b* expression (Extended Data Fig. 6i,j).

To assess whether the changes in the Tau;CL microglia were due to the intrinsic defects in the CL mice, we performed 3D reconstruction of WT and CL microglia (Fig. 6a). We found that the CL microglia had reduced total processes, surface area, cell volume and terminal and branch points compared to WT controls (Fig. 6b). To further evaluate the functional role of these changes in immune activation, we performed i.p. injection of LPS to WT and CL mice and measured the expression of proinflammatory cytokine in hippocampal samples. The CL mutant mice showed significantly less induction of *Tnfa*, *Il1b*, *Il6* and *Irf7* compared to WT controls (Fig. 6c), indicating compromised immune responses in CL mutant. This was also the case when primary microglia cultures were challenged with LPS (Fig. 6d).

To test whether changing lysosomal acidity can directly modulate immune response, we treated primary mixed glia cultures with acidic nanoparticles to acidify the lysosome[23]. Immunostaining showed that the nanoparticles were delivered to LAMP1-positive lysosomes (Extended Data Fig. 7). Cotreatment of the acidic nanoparticles with LPS showed dose-dependent increases of *Tnfa* and *Il1b* expression (Fig. 6e,f). On the contrary, cotreatment of LPS with bafilomycin or chloroquine, both of which are known to increase lysosomal pH, led to greatly diminished *Tnfa* and *Il1b* expression (Fig. 6e,f). These results demonstrate a direct regulation of the immune response by lysosomal pH. Overall, we have established that proper lysosomal acidification mediated by TFEB–v-ATPase signaling is essential for immune activation.

snRNA-seq identified a mTOR/HIF-1 low microglia subcluster

To understand the molecular mechanisms by which TFEB–v-ATPase signaling regulates microglia activity, we carried out snRNA-seq analysis of hippocampus obtained from 9-month-old WT, CL, Tau and Tau;CL littermates (Fig. 7a and Extended Data Fig. 8a,b). Cell type composition analysis showed that, consistent with the Iba1 immunostaining, the expanded microglia population in Tau mice was substantially reduced in Tau;CL (Fig. 7b). Further clustering of microglia identified ten distinct subclusters (Fig. 7c). Based on the expression of marker genes described in Fig. 3, we were able to further divide the homeostatic subcluster 0 into two subpopulations, 0a and 0b, which together with the previously identified subclusters 1 (transitional), 2 (DAM/MGnD-like) and 3 (IFN-responsive), consist of the major microglia subclusters and were analyzed further. Composition analysis of each subcluster across genotypes revealed that subcluster 0a was reduced whereas 0b was expanded in CL mice compared to WT and both were greatly diminished in Tau samples (Fig. 7d,e). Strikingly, subcluster 0b was largely preserved in Tau;CL mice, indicating that this subcluster was unable to be converted to activated states. This effect was observed in both male and female mice, despite slight gender differences in microglia profiles observed in Tau mice (Extended Data Fig. 8c). Analysis of DEGs between WT and CL microglia showed that the majority of genes were downregulated (Extended Data Fig. 9a), suggesting that the expanded subcluster 0b was associated with suppressed gene expression profiles. Further analysis of subcluster 0b with 0a revealed that the downregulated genes include the lysosome (Fig. 7g), mTOR (Fig. 7h) and Hypoxia Inducible Factor-1 (HIF-1) (Fig. 7i) signaling pathways. In contrast, these pathway genes were prominently upregulated in both subclusters 2 and 3, and to a lesser degree in subcluster 1, compared with subcluster 0a (Fig. 7g–i). These results indicate that microglia in subcluster 0b were refractory to initiate the activation process in tauopathy conditions, due to lower lysosomal activity and possibly associated mTOR and HIF-1 signaling pathways (Fig. 7j).

Consistent with this notion, comparison between Tau and Tau;CL microglia showed that the preservation of subcluster 0b in Tau;CL was correlated with drastically reduced subclusters 1, 2 and 3 (Fig. 7d,e). Accordingly, the upregulated DEGs identified in Tau microglia, including lysosome, immune and lipid metabolic pathway genes, were markedly reduced in Tau;CL (Fig. 8a,b and Extended Data Fig. 9b,c). In agreement with the subcluster analysis, the mTOR and HIF-1 signaling pathways were upregulated in Tau but downregulated in CL and Tau;CL microglia (Fig. 8c,d). The gene expression changes were corroborated by immunostaining for HIF-1α, a subunit of HIF-1, showing upregulated HIF-1α immunoreactivity in Iba1-marked microglia in Tau mice, which was significantly reduced in Tau;CL samples (Fig. 8e,f). To test a functional role of HIF-1 signaling in microglia activation, we stimulated the primary microglia cultures with LPS, which significantly induced the expression of *Hif1a* (Fig. 8g) and proinflammatory cytokine genes *Il1b* and *Il6* (Fig. 8h,i). Cotreatment with a HIF-1α inhibitor Chrysin suppressed the LPS-induced *Il1b* and *Il6* expression (Fig. 8h,i). The efficacy of Chrysin in HIF-1α inactivation was demonstrated by the reduction of HIF-1α and downstream targets *Vegf* and *Pgk1* induced by hypoxia mimetic $CoCl_2$ (Extended Data Fig. 10).

Fig. 4 | Generation of an in vivo model of lysosomal dysfunction through CLEAR mutagenesis. a, Dotplot showing the relative gene expression levels of the v-ATPase subunits in microglia of WT and Tau mice. **b**, The consensus TFEB-binding CLEAR motif (upper panel). WT: two canonical CLEAR sequences in the promoter of *Atp6v1h*. CL: mutated CLEAR motif with the altered base pairs highlighted. **c**, Chromatin immunoprecipitation and qPCR analysis (ChIP-PCR) of N2a cells transfected with TFEB-FLAG or GFP-FLAG with an anti-FLAG antibody. **d**, Luciferase assay in HEK293 cells cotransfected with TFEB, WT or CL mutant *Atp6v1h* promoter-driven firefly luciferase construct and the Renilla construct. AQP1 is a promoter construct that does not contain a CLEAR sequence. **e**, Luciferase assay demonstrating that insoluble tau promotes *Atp6v1h* transcription. Cells were cotransfected with CMV or Tau-P301L vector (Tau) with the wild-type *Atp6v1h* promoter luciferase and Renilla vectors. Tau + Pff: Pff was added for seeding insoluble tau. **f**, The same luciferase assay showed that Tau + Pff failed to activate the luciferase activity when the CL protomer was used. **g**, CL mutant mice exhibit a specific reduction in *Atp6v1h* transcript without affecting other TFEB lysosomal targets. qPCR analysis of forebrain RNA extract from 1-month-old CL or WT control. $n = 4$ per group. **h**, Western blotting with quantification of ATP6V1H protein levels in forebrain lysates of 9-month-old WT and CL mice. $n = 4$ per group. **i**, qPCR analysis of *Atp6v1h* transcripts in WT and CL primary glial cultures under basal (Ctrl), Torin-treated (Torin) or starvation (Starve) conditions. **j**, Representative images of LysoSensor Green DND-189 fluorescence in WT and CL primary glial cultures. Bafilomycin (Baf) and NH_4Cl-treated WT cultures were used as controls. **k**, Quantification of **j**. $n = 5$ per group. **l**, Representative images of DQ-BSA fluorescence costained with LAMP1 in WT and CL primary glial cultures. $n = 8$ per group. **m**, Quantification of **l**. Scale bar, 10 µm. Data are presented as average ± s.em. One-way ANOVA with Sidak's correction (**d**,**e**,**f**,**i**,**k**,**m**) and two-tailed *t*-test (**c**,**g**,**h**). Each in vitro experiment was repeated three times with each in triplicate. See also Extended Data Fig. 3.

https://doi.org/10.1038/s41593-023-01494-2

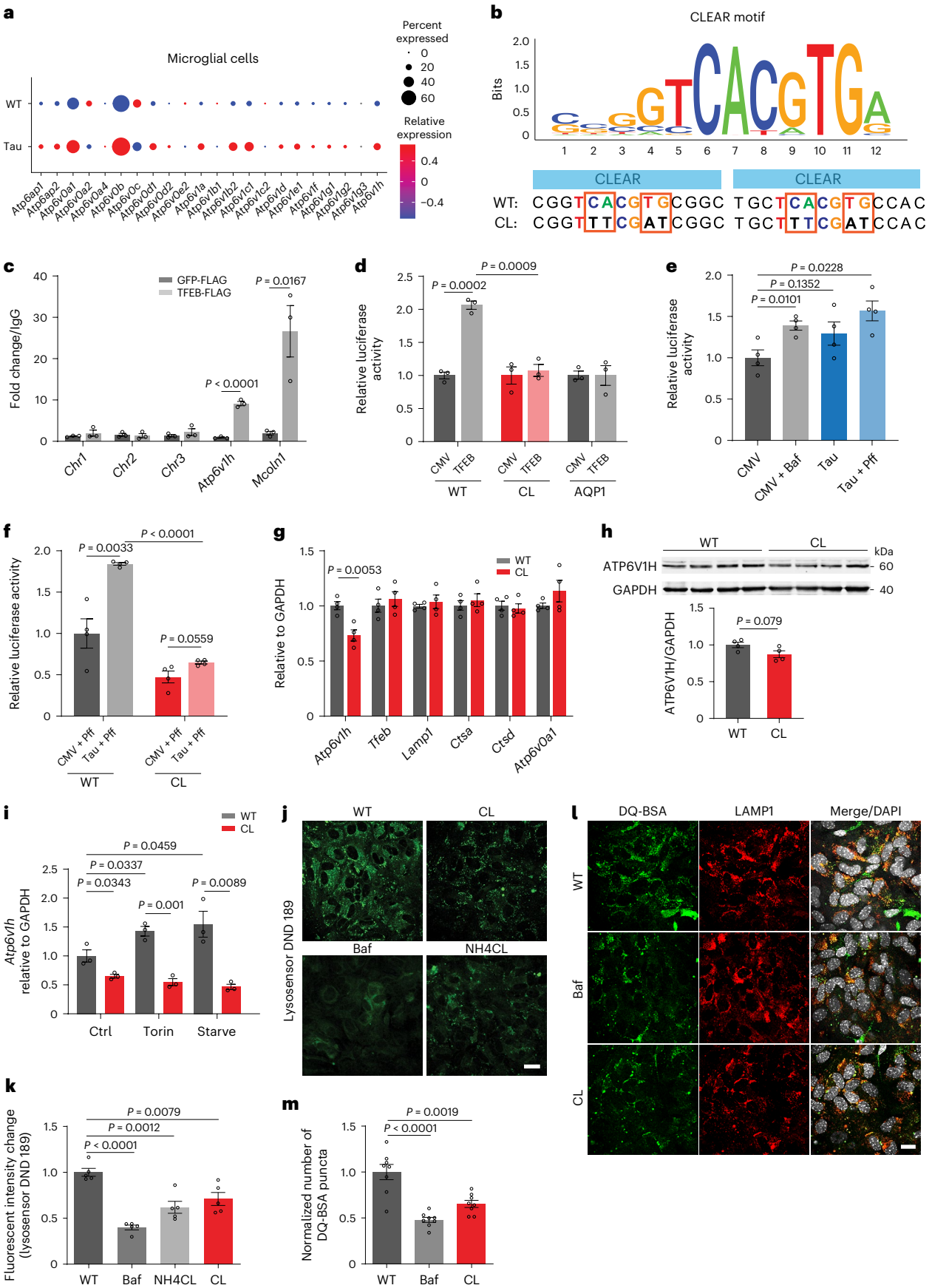

https://doi.org/10.1038/s41593-023-01494-2

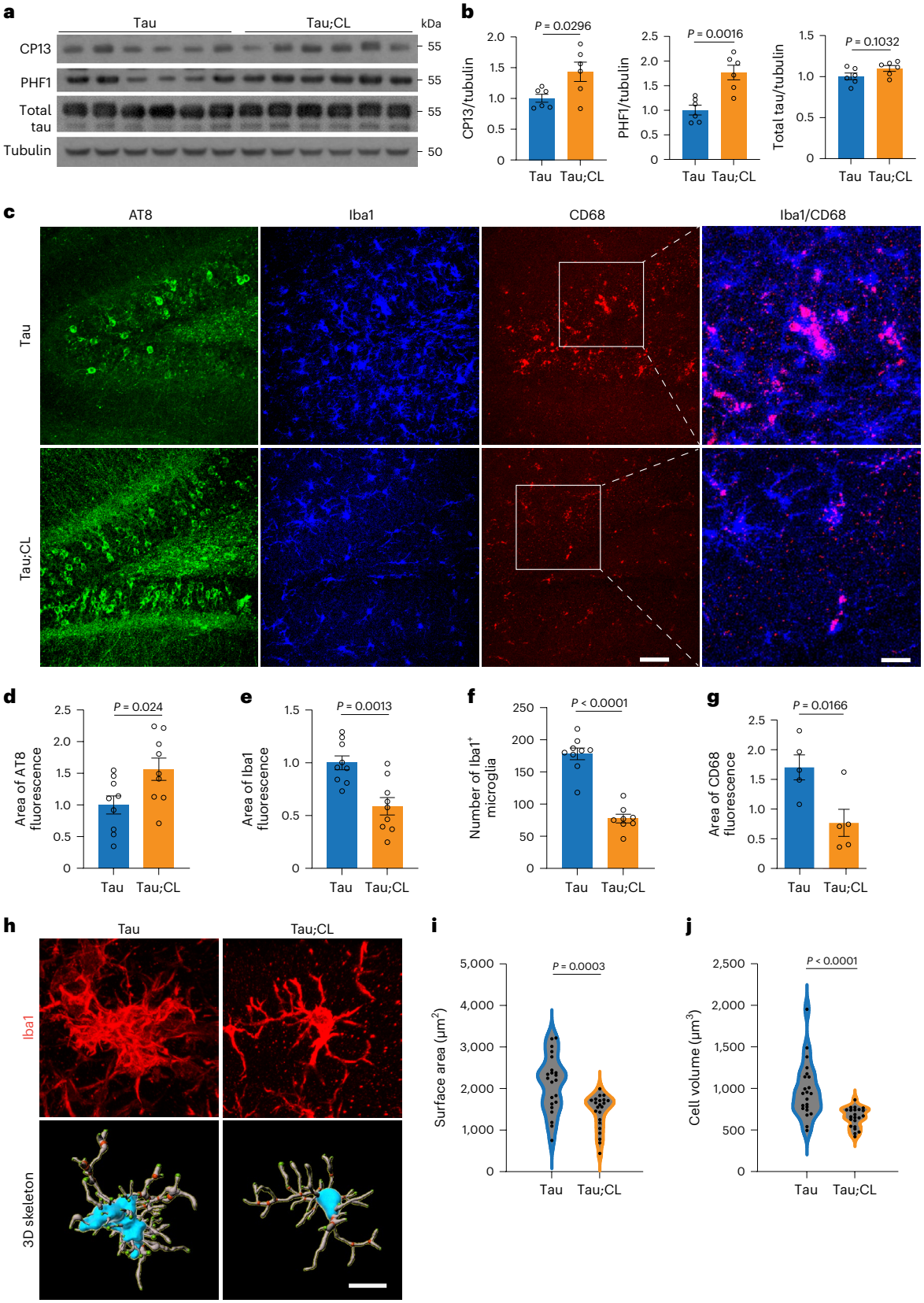

Fig. 5 | Increased phospho-tau and decreased gliosis in Tau mice crossed to CL background. a,**b**, Western blot (**a**) with quantification (**b**) of total and phospho-tau species recognized by PHF1 and CP13 antibodies from forebrain lysates of 9-month-old Tau mice or Tau mice homozygous for the CL mutation (Tau;CL). $n = 6$ per group. **c**–**g**, Representative fluorescent confocal images of AT8, Iba1 and CD68 immunostaining (**c**) with quantification of AT8 (**d**), Iba1 fluorescence area (**e**), Iba1-positive cells (**f**) and CD68 fluorescence area (**g**) in the dentate gyrus samples of 9-month-old Tau and Tau;CL mice. Scale bars, 50 μm (for AT8, Iba1 and CD68) and 20 μm in brackets (for Iba1/CD68). $n = 9$ per genotype in **d** and **e**; $n = 9$ (Tau) and $n = 8$ (Tau;CL) in **f**; $n = 5$ per genotype in **g**. **h**, Representative Iba1 staining and 3D skeletonization of microglia in the hippocampus of Tau and Tau;CL mice. Scale bar, 10 μm. **i**,**j**, Quantification of microglia surface area (**i**) and volume (**j**) per cell using the IMARIS software. $n = 6$ per group. Data are presented as average ± s.e.m. Two-tailed Student's *t*-test. See also Extended Data Figs. 4–6.

https://doi.org/10.1038/s41593-023-01494-2

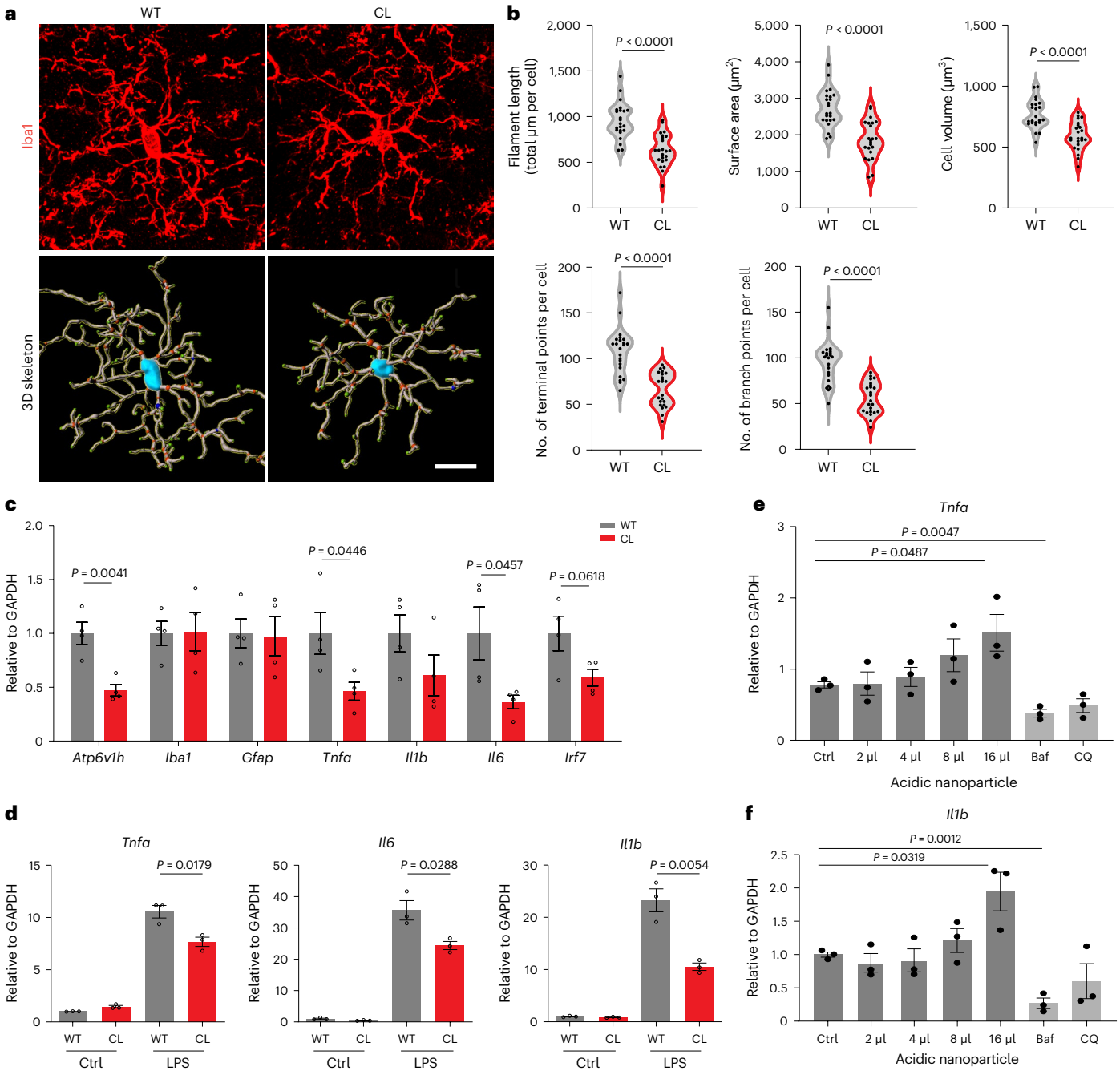

Fig. 6 | Disruption of TFEB–v-ATPase lysosomal signaling leads to impaired microglia morphology and activation. a, Representative Iba1 staining and 3D skeletonization of microglia in the hippocampus of WT and CL mice. Red dots mark branching points of microglia processes; green dots mark terminal points. Scale bar, 10 µm. **b**, Quantification of microglia filament length, surface area, volume, terminal points and branch points using the IMARIS software. $n = 4$ per group. **c**, qPCR analysis of proinflammatory cytokine expression in hippocampus tissues of 4-month-old WT and CL mice injected with LPS. $n = 4$ per genotype. **d**, qPCR analysis of proinflammatory cytokine expression in primary microglia cultures generated from WT and CL pups at basal conditions (Ctrl) and with LPS stimulation. **e**,**f**, qPCR analysis of *Tnfa* (**e**) or *Il1b* (**f**) levels of primary microglia cultures treated with LPS together with increasing doses of acidic nanoparticles to increase lysosomal acidity, or bafilomycin (Baf) or chloroquine (CQ) to reduce lysosomal acidity, showing that modulation of lysosomal acidity directly leads to altered proinflammatory cytokine expression. Data are presented as average ± s.e.m. One-way ANOVA with Sidak's correction (**e**,**f**) and two-tailed Student's *t*-test (**b**–**d**). Each in vitro experiment was repeated three times with each in triplicate. See also Extended Data Fig. 7.

Discussion

Lysosomes play essential roles in cellular homeostasis through the LYNUS system and the coordinated mTOR-TFEB lysosome to nucleus signaling[24]. Besides the lysosomal genes, TFEB also regulates the transcription of a broad range of other targets[25,26], making it difficult to decipher a lysosome-specific mechanism. To tackle this problem, we chose to specifically manipulate the TFEB–v-ATPase pathway through CLEAR mutagenesis of the *Atp6v1h* subunit, given the crucial role of v-ATPase in regulating lysosomal pH and function, without altering TFEB or affecting any of the other TFEB targets. We report that the TFEB–*Atp6v1h* transcriptional program is essential in regulating v-ATPase activity and lysosomal acidification and function under physiological conditions. Combined with the *Drosophila* study[14,15], these results support the notion that TFEB–v-ATPase signaling represents an evolutionarily

https://doi.org/10.1038/s41593-023-01494-2

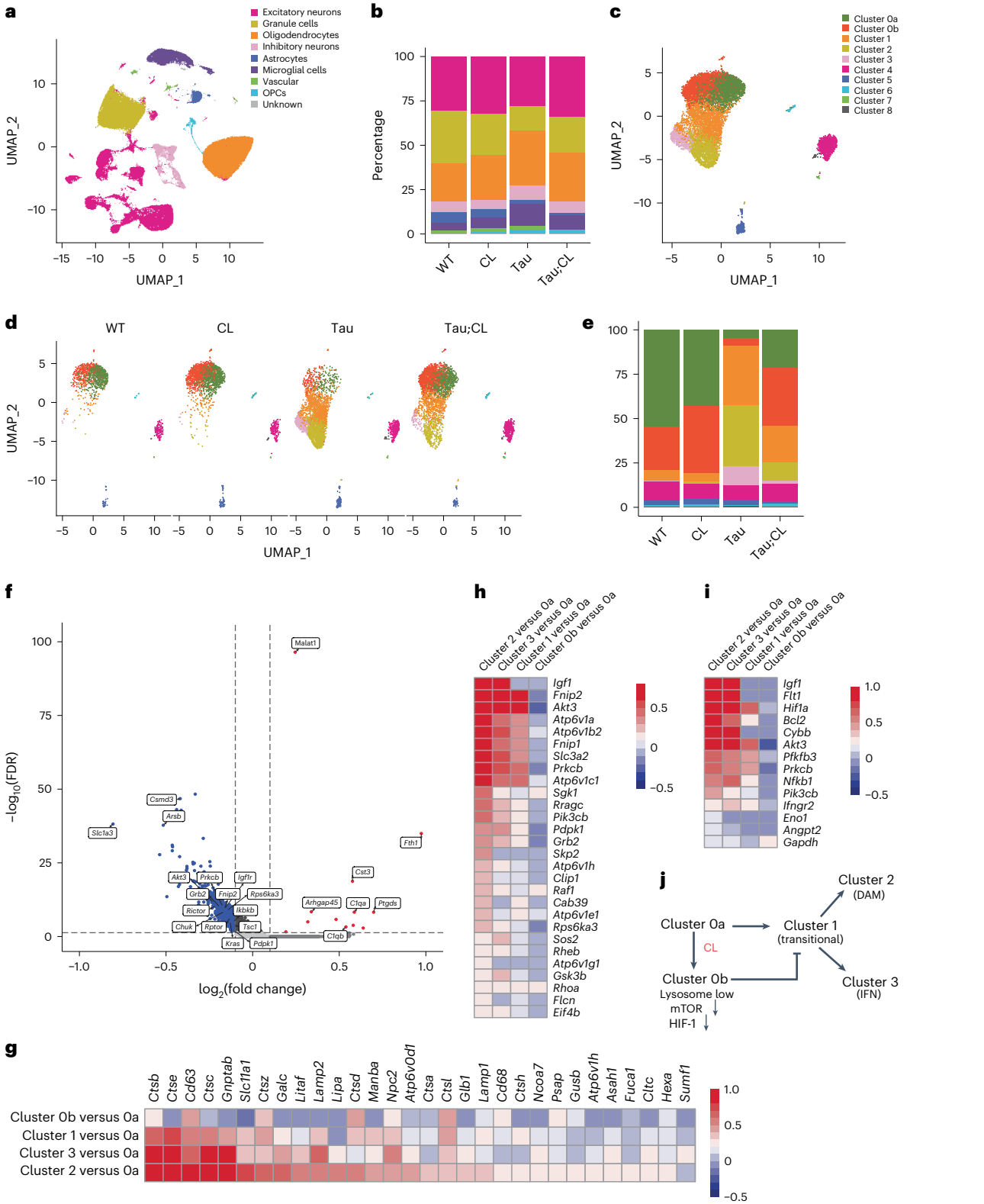

Fig. 7 | snRNA-seq analysis identified a distinct homeostatic microglia subcluster regulated by TFEB–v-ATPase. a, UMAP representation of snRNA-seq analysis of 137,734 cells from hippocampus of WT, CL, Tau and Tau;CL mice. **b**, Stacked barplot showing cell type compositions across different genotypes. The bars are colored by their corresponding cell classes as labeled in **a**. **c**, UMAP representation of reclustered microglia cells, with further separation of subcluster 0 to 0a and 0b. **d**, UMAP representation of reclustered microglia cells across genotypes. Subcluster annotation indicated by colors shown in **c**. **e**, Stacked barplot showing subcluster compositions of microglia across different genotypes. The bars are colored by their corresponding cell classes as labeled in **c**. **f**, Volcano plot showing DEGs for cluster 0b versus cluster 0a. Upregulated genes are highlighted in red; downregulated genes are highlighted in blue. Significantly downregulated DEGs in mTOR pathway are labeled. **g**–**i**, Heatmaps comparing the levels of lysosome (**g**), mTOR (**h**) and HIF-1 (**i**) signaling pathway-related genes (log_2(fold change)) in different microglia subclusters. **j**, A model illustrating microglia subcluster relationships. Microglia in subclusters 0b with lower lysosomal, mTOR and HIF-1 activities are refractory to transition toward activated microglia subcluster 2 and 3 upon activation; loss of TFEB–v-ATPase regulation (CL) drives the expansion of homeostatic subcluster 0b at the expense of subcluster 0a. See also Extended Data Figs. 8–10.

conserved mechanism in maintaining lysosomal homeostasis. Importantly, we demonstrate a critical role of this pathway in microglia state transition. Disruption of TFEB lysosomal function through v-ATPase locks microglia in a unique resting state with downregulated mTOR and HIF-1 metabolic pathways that are incapable of mounting an innate immune response under stress conditions triggered by mutant tau perturbation (Fig. 8j).

The v-ATPase is a multisubunit complex composed of V1 and V0 domains, which carries out ATP hydrolysis and proton entry to the lysosomal lumen, respectively. These subunits cooperate to participate in v-ATPase assembly and function through their unique roles[27]. They may also be subject to differential regulation by TFEB, evidenced by the differences in their CLEAR motifs and TFEB-binding affinities. Therefore, whether disruption of TFEB interaction with other v-ATPase components will result in similar lysosomal phenotypes as ATP6V1H is not clear. Of note, ATP6V1H is a regulatory subunit required for ATP hydrolysis but not complex assembly[28,29]. Mice with *Atp6v1h* haploinsufficiency exhibit increased lysosomal pH and impaired bone remodeling, leading to osteoporosis[30]. In contrast, inactivation of *Atp6v0d2* results in increased bone mass due to enhanced bone formation[31]. The differential phenotypes presented in loss-of-function mouse models are in agreement with the association of the mutations of different v-ATPase subunits with distinct human diseases[2]. In this regard, an intronic *ATP6V1H* variant rs1481950 in humans has been reported to influence BACE1 levels in cerebrospinal fluid, implicating a possible role of ATP6V1H in AD pathogenesis[32].

We demonstrate that TFEB binds to the CLEAR sequence in the *Atp6v1h* promoter and mediates its transcription. This represents part of its expression regulation as mutagenizing the CLEAR sequence only results in ~30% reduction of *Atp6v1h* mRNA levels. Remarkably, this mild reduction is sufficient to alter the entire v-ATPase and lysosomal activity. This is contrasted by the germline *Atp6v1h* heterozygous mice where no lysosomal defects can be detected despite a 50% reduction in *Atp6v1h* mRNA and protein levels. This is likely due to genetic compensation triggered by the steady-state *Atp6v1h* reduction, which becomes ineffective under specific disruption of CLEAR-dependent transcriptional regulation. It is worth noting that the normal lysosomal pH in mixed glia cultures of *Atp6v1h* heterozygous mice is distinct from the reduced lysosomal acidity reported in *Atp6v1h* heterozygous osteoclasts[30]. The differences possibly lie in the high v-ATPase demand in osteoclasts to control extracellular acidification and bone resorption that overcome the threshold of genetic compensation[33].

TFEB belongs to the MiT/TFE family of transcription factors that also includes microphthalmia-associated transcription factor (MITF), transcription factor 3 (TFE3) and transcription factor EC (TFEC). These transcription factors may play redundant roles either through binding to the same consensus CLEAR motifs or upon homo- or heterodimerization among each other[34,35]. Although we used TFEB to examine *Atp6v1h* CLEAR interaction, it is possible that other TFEB homologs also bind to the same sequence and contribute to the CL mutant phenotypes. Of particular interest, MITF has been shown to be enriched in AD microglia and control both DAM signatures and phagocytosis[36]. The specific roles of these factors in v-ATPase signaling and lysosomal function warrant further investigation.

Our bulk brain RNA sequencing identified upregulation of TFEB and the lysosomal pathway in Tau mice. Using in vitro assays, we showed that insoluble tau promotes TFEB nuclear translocation and downstream gene expression. This effect may be caused directly by the intracellular tau aggregates as TFEB can be activated by various cellular stress and damage signals[25]. Alternatively, this may be triggered by tau-induced lysosomal stress as tau is known to be degraded in the lysosome[11]. Although the precise mechanism remains to be established, the fact that reducing the v-ATPase and lysosomal pathway in CL leads to worsened tau pathology supports the idea that the lysosomal pathway upregulation in Tau mice represents an innate adaptive response against pathological tau accumulation. However, this protective mechanism may no longer be effective under chronic tauopathy conditions, necessitating the addition of exogenous TFEB to resolve the increasing tau burden[8,12].

snRNA-seq analysis of PS19 Tau mice confirmed the transcriptomic changes reported previously[37,38], revealing drastically altered microglia profiles with diminished homeostatic microglia (subcluster 0) and corresponding expansion of transitional subcluster 1, which then converts to two distinct subpopulations: DAM/MGnD-like (subcluster 2) and IFN-responsive (subcluster 3). The elevated lysosomal pathway is a prominent feature of DAM[17]. A recent study showed that, in a combined Tau and APOE mouse model, TREM2-independent DAM gene upregulation involves TFEB–CLEAR network following increased lysosomal burden[39]. These findings together suggest that TFEB-associated lysosomal gene signature is a component of the general microglia activation program in response to pathological stimuli in the brain. Critically, our result that tuning down the CLEAR network-dependent lysosomal pathway in Tau;CL microglia leads to impaired glial and immune activation demonstrates that lysosomal pathway upregulation is required to induce microglia activation. In this regard, TFEB has been shown to influence immune response through its regulation of the autophagy–lysosomal pathway and by direct transcriptional activation of immune target genes[26]. Although these mechanisms may indeed be at play, our data that immune activity can be directly regulated by specific TFEB–v-ATPase lysosomal signaling without affecting TFEB or its inflammation targets highlight an essential role of the lysosome in immune system regulation.

Subclustering analysis of WT and CL microglia allowed us to further divide the homeostatic subcluster into two populations, 0a and 0b, with 0b enriched in CL microglia. This subcluster expresses low lysosomal genes and is associated with reduced mTOR and HIF-1 signaling pathways. Notably, subcluster 0b failed to be converted to activated states on Tau background and, therefore, is locked in the homeostatic state. Indeed, the microglial phenotypes observed in the Tau;CL mice recapitulate key features of *Trem2* knockout on amyloid mouse models, with both displaying defective microglia activation, reduced DAM signatures and impaired mTOR activity[40,41]. Since we did not detect changes of *Trem2* expression in Tau microglia, we propose that mTOR may serve as a common mediator converging membrane receptor signaling and lysosomal activity to microglial activation.

mTOR plays a central role in cellular metabolism in multiple cell types, including innate immune cells, through regulating several downstream pathways, among them the HIF-1 signaling pathway[42,43]. The activation of microglia requires a metabolic switch from oxidative phosphorylation to aerobic glycolysis to swiftly generate energy for fulfillment of energy-intensive processes such as migration, cytokine production and secretion, phagocytosis and proliferation. HIF-1α

Fig. 8 | Disruption of TFEB–v-ATPase regulation leads to compromised lysosomal and inflammatory changes and reduced mTOR and HIF-1 signaling in tauopathy. a, KEGG enrichment analysis for upregulated genes comparing Tau;CL with Tau. Hypergeometric test was used to identify significant enrichment pathways; FDR < 0.01. **b**, Venn diagram summarizing the numbers of upregulated genes for all microglia in Tau and Tau;CL. **c**,**d**, Heatmaps comparing mTOR (**c**) and HIF-1 (**d**) signaling pathway-related genes ($\log_2$(fold change)) between different genotypes. **e**, Representative images of 9-month-old WT, CL, Tau and Tau;CL brains stained for HIF-1α (red) and Iba1 (green). Scale bars, 50 μm; 25 μm in zoomed images. **f**, Quantification of mean fluorescence intensity per cell of HIF-1α staining in WT, CL, Tau and Tau;CL mice (n = 50 cells/group). **g**–**i**, qPCR analysis of *Hif1a* (**g**), *Il1b* (**h**) and *Il6* (**i**) levels in microglia cultures treated with LPS or LPS + HIF-1α inhibitor Chrysin. n = 3 independent experiments. **j**, Diagram depicting the mechanism of microglia activation in Tau mice mediated by TFEB–v-ATPase lysosomal regulation. Data are presented as average ± s.e.m. Two-tailed Student's t-test. See also Extended Data Fig. 10.

https://doi.org/10.1038/s41593-023-01494-2

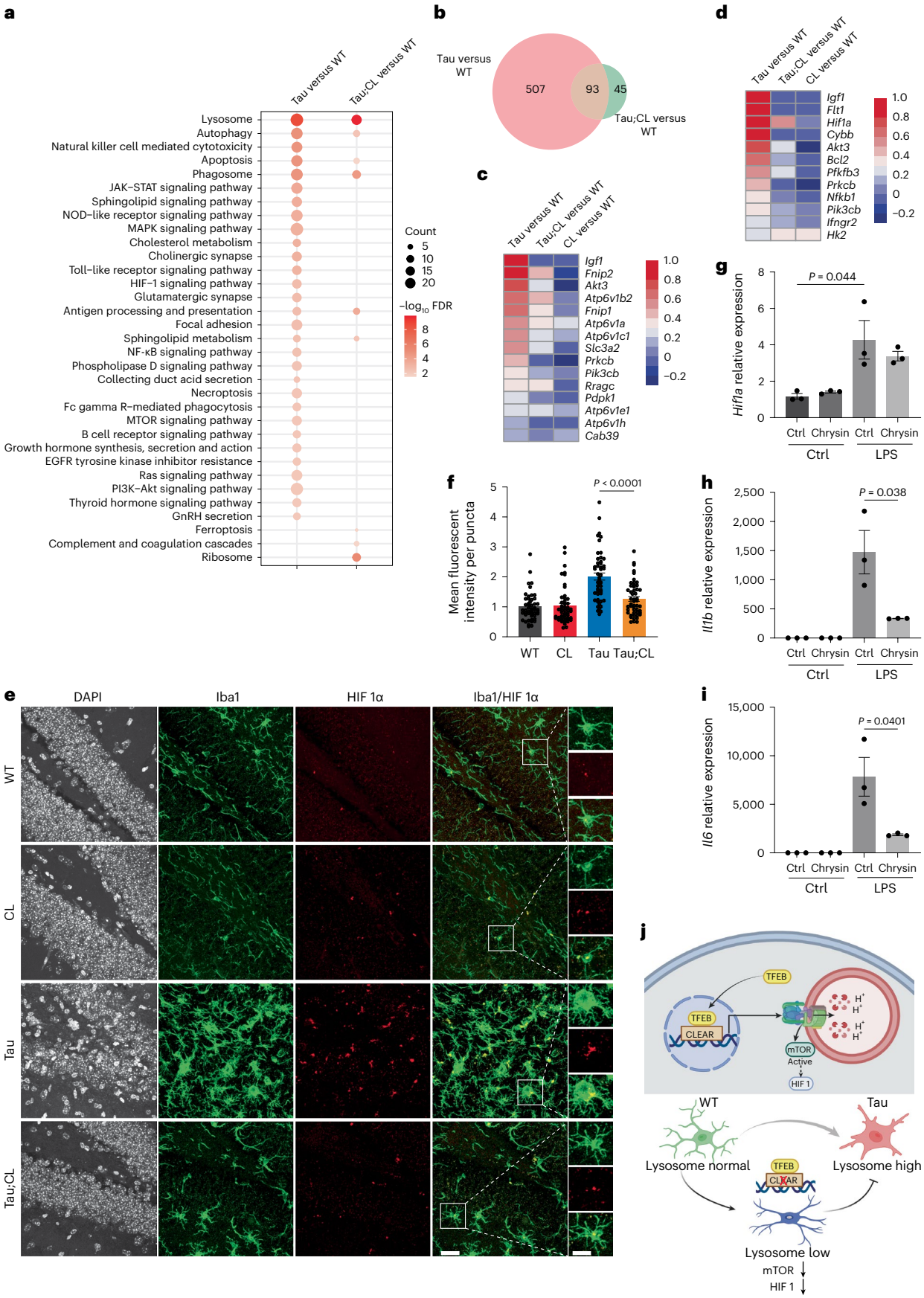

is a canonical modulator of metabolic reprogramming[44]. We found significantly increased HIF-1 signaling pathway genes in fully activated microglia subclusters and elevated HIF-1α immunostaining in microglia of Tau mice, both of which were reduced by CL, supporting an involvement of the HIF-1 pathway in microglial activation. As an mTOR downstream target, reduced HIF-1 signaling may be caused by dampened mTOR, although it is also possible that this event is mTOR independent. Besides HIF-1, mTOR can modulate innate inflammatory responses by acting on the type I IFN pathway and cytokine production via STAT3 and NF-κB[45]. Consistent with the reported role of microglial NF-κB in tauopathy[46], we found that the JAK-STAT and NF-κB signaling pathways were among the top altered cellular immune response pathways in microglia of Tau mice, both of which were drastically reduced in Tau;CL microglia. Overall, the markedly reduced mTOR pathway in the microglia subcluster enriched in CL and Tau;CL mice indicate that TFEB–v-ATPase dysregulation not only affects lysosomal acidification and degradative capacity but also impairs mTOR activation, resulting in its inability to undergo the metabolomic reprogramming required for microglia activation through HIF-1 and possibly other immune pathways.

It is well-established that TFEB responds to mTOR and the LYNUS machinery composed of v-ATPase to undergo cytoplasmic to nucleus trafficking. Our work reveals that nuclear TFEB regulates the v-ATPase transcriptional program, specifically through the CLEAR-dependent *Atp6v1h* gene expression, which in turn feeds back to regulate lysosomal pH and function and the mTOR pathway. This feedback regulatory pathway is not only important for intraneuronal tau clearance but also for microglia activation in response to tau pathology. These findings demonstrate a critical role of the lysosome, in part modulated by TFEB–v-ATPase signaling, in both neuronal and immune cell function in physiology and diseases of tauopathy.

Limitations of the study

Our work has several limitations. Firstly, the CLEAR mutation is introduced in all cell types, thus the neuronal and microglia phenotypes may be the result of cell-intrinsic effect within these cells or the consequences of cell–cell interactions. The creation of a microglia-specific mutant will be desirable in this regard. Secondly, whereas our analysis focused on cell-autonomous mechanisms of microglia, the TFEB lysosomal pathway may also regulate immune pathways in other cell types, such as astrocytes and peripheral immune cells, which may also contribute to the phenotypes observed in the CLEAR mutant. Of particular relevance, astrocyte reactivity marked by GFAP immunofluorescence is also reduced in Tau;CL mice, and a recent study suggested a critical role of T cell infiltration in microglia and immune regulation in tauopathy[47]. Therefore, the central versus peripheral and cell-autonomous versus noncell-autonomous role of the TFEB–v-ATPase signaling require further investigation. Thirdly, microglia are known to undergo dynamic changes. We analyzed our mice at 9 months of age when robust tau pathology and immune phenotype have already developed. Additional analysis at earlier time points will allow better understanding of the lysosomal regulation of microglia dynamics. Lastly, like many other studies, we used the PS19 (Tau) transgenic mice to model tauopathy. These mice express the P301S mutant tau, whereas only WT tau is expressed in human AD. Moreover, the granule cell loss in the dentate gyrus of Tau and Tau;CL mice could confound tauopathy-induced microglia signatures. Therefore, to what degree the finding can be applied to human AD requires further scrutinization.

Online content

Any methods, additional references, Nature Portfolio reporting summaries, source data, extended data, supplementary information, acknowledgements, peer review information; details of author contributions and competing interests; and statements of data and code availability are available at https://doi.org/10.1038/s41593-023-01494-2.

References

1. Ballabio, A. & Bonifacino, J. S. Lysosomes as dynamic regulators of cell and organismal homeostasis. *Nat. Rev. Mol. Cell Biol.* **21**, 101–118 (2020).
2. Colacurcio, D. J. & Nixon, R. A. Disorders of lysosomal acidification—the emerging role of v-ATPase in aging and neurodegenerative disease. *Ageing Res. Rev.* **32**, 75–88 (2016).
3. Settembre, C., Fraldi, A., Medina, D. L. & Ballabio, A. Signals from the lysosome: a control centre for cellular clearance and energy metabolism. *Nat. Rev. Mol. Cell Biol.* **14**, 283–296 (2013).
4. Sardiello, M. et al. A gene network regulating lysosomal biogenesis and function. *Science* **325**, 473–477 (2009).
5. Settembre, C. et al. TFEB links autophagy to lysosomal biogenesis. *Science* **332**, 1429–1433 (2011).
6. Palmieri, M. et al. Characterization of the CLEAR network reveals an integrated control of cellular clearance pathways. *Hum. Mol. Genet.* **20**, 3852–3866 (2011).
7. Xiao, Q. et al. Enhancing astrocytic lysosome biogenesis facilitates Aβ clearance and attenuates amyloid plaque pathogenesis. *J. Neurosci.* **34**, 9607–9620 (2014).
8. Polito, V. A. et al. Selective clearance of aberrant tau proteins and rescue of neurotoxicity by transcription factor EB. *EMBO Mol. Med.* **6**, 1142–1160 (2014).
9. Parr, C. et al. Glycogen synthase kinase 3 inhibition promotes lysosomal biogenesis and autophagic degradation of the amyloid-β precursor protein. *Mol. Cell. Biol.* **32**, 4410–4418 (2012).
10. Xiao, Q. et al. Neuronal-targeted TFEB accelerates lysosomal degradation of APP, reducing Aβgeneration and amyloid plaque pathogenesis. *J. Neurosci.* **35**, 12137–12151 (2015).
11. Xu, Y. et al. TFEB regulates lysosomal exocytosis of tau and its loss of function exacerbates tau pathology and spreading. *Mol. Psychiatry* **26**, 5925–5939 (2021).
12. Martini-Stoica, H. et al. TFEB enhances astroglial uptake of extracellular tau species and reduces tau spreading. *J. Exp. Med.* **215**, 2355–2377 (2018).
13. Mindell, J. A. Lysosomal acidification mechanisms. *Annu Rev. Physiol.* **74**, 69–86 (2012).
14. Bouché, V. et al. Drosophila Mitf regulates the V-ATPase and the lysosomal-autophagic pathway. *Autophagy* **12**, 484–498 (2016).
15. Zhang, T. et al. Mitf is a master regulator of the v-ATPase, forming a control module for cellular homeostasis with v-ATPase and TORC1. *J. Cell Sci.* **128**, 2938–2950 (2015).
16. Xu, Y., Martini-Stoica, H. & Zheng, H. A seeding based cellular assay of tauopathy. *Mol. Neurodegener.* **11**, 32 (2016).
17. Keren-Shaul, H. et al. A unique microglia type associated with restricting development of Alzheimer's disease. *Cell* **169**, 1276–1290.e1217 (2017).
18. Krasemann, S. et al. The TREM2-APOEpathway drives the transcriptional phenotype of dysfunctional microglia in neurodegenerative diseases. *Immunity* **47**, 566–581.e569 (2017).
19. Pastore, N. et al. TFEB and TFE3 cooperate in the regulation of the innate immune response in activated macrophages. *Autophagy* **12**, 1240–1258 (2016).
20. Settembre, C. et al. A lysosome-to-nucleus signalling mechanism senses and regulates the lysosome via mTOR and TFEB. *EMBO J.* **31**, 1095–1108 (2012).
21. Martina, J. A., Chen, Y., Gucek, M. & Puertollano, R. MTORC1 functions as a transcriptional regulator of autophagy by preventing nuclear transport of TFEB. *Autophagy* **8**, 903–914 (2012).
22. Roczniak-Ferguson, A. et al. The transcription factor TFEB links mTORC1 signaling to transcriptional control of lysosome homeostasis. *Sci. Signal* **5**, ra42 (2012).
23. Zeng, J., Shirihai, O. S. & Grinstaff, M. W. Degradable nanoparticles restore lysosomal pH and autophagic flux in lipotoxic pancreatic beta cells. *Adv. Health. Mater.* **8**, e1801511 (2019).

24. Martini-Stoica, H., Xu, Y., Ballabio, A. & Zheng, H. The autophagy-lysosomal pathway in neurodegeneration: a TFEB perspective. *Trends Neurosci.* **39**, 221–234 (2016).
25. Martina, J. A., Diab, H. I., Brady, O. A. & Puertollano, R. TFEB and TFE3 are novel components of the integrated stress response. *EMBO J.* **35**, 479–495 (2016).
26. Brady, O. A., Martina, J. A. & Puertollano, R. Emerging roles for TFEB in the immune response and inflammation. *Autophagy* **14**, 181–189 (2018).
27. Toei, M., Saum, R. & Forgac, M. Regulation and isoform function of the V-ATPases. *Biochemistry* **49**, 4715–4723 (2010).
28. Ho, M. N. et al. VMA13 encodes a 54-kDa vacuolar H(+)-ATPase subunit required for activity but not assembly of the enzyme complex in Saccharomyces cerevisiae. *J. Biol. Chem.* **268**, 18286–18292 (1993).
29. Jefferies, K. C. & Forgac, M. Subunit H of the vacuolar (H+) ATPase inhibits ATP hydrolysis by the free V1 domain by interaction with the rotary subunit F. *J. Biol. Chem.* **283**, 4512–4519 (2008).
30. Duan, X. et al. Deficiency of ATP6V1H causes bone loss by inhibiting bone resorption and bone formation through the TGF-β1 pathway. *Theranostics* **6**, 2183–2195 (2016).
31. Lee, S. H. et al. v-ATPase V0 subunit d2-deficient mice exhibit impaired osteoclast fusion and increased bone formation. *Nat. Med.* **12**, 1403–1409 (2006).
32. Hu, H. et al. Genome-wide association study identified ATP6V1H locus influencing cerebrospinal fluid BACE activity. *BMC Med. Genet.* **19**, 75 (2018).
33. Duan, X., Yang, S., Zhang, L. & Yang, T. V-ATPases and osteoclasts: ambiguous future of V-ATPases inhibitors in osteoporosis. *Theranostics* **8**, 5379–5399 (2018).
34. Fisher, D. E., Carr, C. S., Parent, L. A. & Sharp, P. A. TFEB has DNA-binding and oligomerization properties of a unique helix-loop-helix/leucine-zipper family. *Genes Dev.* **5**, 2342–2352 (1991).
35. Hemesath, T. J. et al. microphthalmia, a critical factor in melanocyte development, defines a discrete transcription factor family. *Genes Dev.* **8**, 2770–2780 (1994).
36. Dolan, M.-J. et al. A resource for generating and manipulating human microglial states in vitro. Preprint at *bioRxiv* https://doi.org/10.1101/2022.05.02.490100 (2022).
37. Shi, Y. et al. Overexpressing low-density lipoprotein receptor reduces tau-associated neurodegeneration in relation to apoE-linked mechanisms. *Neuron* **109**, 2413–2426.e2417 (2021).
38. Udeochu, J. C. et al. Tau activation of microglial cGAS–IFN reduces MEF2C-mediated cognitive resilience. *Nat. Neurosci.* **26**, 737–750 (2023).
39. Gratuze, M. et al. TREM2-independent microgliosis promotes tau-mediated neurodegeneration in the presence of ApoE4. *Neuron* **111**, 202–219.e207 (2023).
40. Wang, Y. et al. TREM2 lipid sensing sustains the microglial response in an Alzheimer's disease model. *Cell* **160**, 1061–1071 (2015).
41. Ulland, T. K. et al. TREM2 maintains microglial metabolic fitness in Alzheimer's disease. *Cell* **170**, 649–663.e613 (2017).
42. Düvel, K. et al. Activation of a metabolic gene regulatory network downstream of mTOR complex 1. *Mol. Cell* **39**, 171–183 (2010).
43. Weichhart, T., Hengstschläger, M. & Linke, M. Regulation of innate immune cell function by mTOR. *Nat. Rev. Immunol.* **15**, 599–614 (2015).
44. Kierans, S. J. & Taylor, C. T. Regulation of glycolysis by the hypoxia-inducible factor (HIF): implications for cellular physiology. *J. Physiol.* **599**, 23–37 (2021).
45. Weichhart, T. et al. The TSC-mTOR signaling pathway regulates the innate inflammatory response. *Immunity* **29**, 565–577 (2008).
46. Wang, C. et al. Microglial NF-κB drives tau spreading and toxicity in a mouse model of tauopathy. *Nat. Commun.* **13**, 1969 (2022).
47. Chen, X. et al. Microglia-mediated T cell infiltration drives neurodegeneration in tauopathy. *Nature* **615**, 668–677 (2023).

Methods

Animals

All protocols involving mice were approved by the Institutional Animal Care and Use Committee of Baylor College of Medicine. PS19 (Tau) mice were obtained from Jackson Labs (008169)[48]. Heterozygotes were bred to B6C3F1/J wild-type mice to maintain the line. CL mice were generated utilizing CRISPR-mediated mutagenesis as described below. Both sexes were used throughout the study.

CRISPR–Cas9-mediated mutagenesis design and CL mouse production

To introduce the mutagenized CLEAR sequence site in *Atp6v1h*, a single guide RNA (sgRNAs) was selected using the Wellcome Trust Sanger Institute Genome Editing website (http://www.sanger.ac.uk/htgt/wge/), so that a double-strand break by the resulting sgRNA/Cas9 complex would be created as proximal to the CLEAR sequence site as possible (https://www.sanger.ac.uk/htgt/wge/crispr/300195847). Homology-mediated repair of the double-strand break would be directed by a single-stranded donor DNA containing the mutagenized CLEAR site. The sgRNA was synthesized using DNA templates for in vitro transcription. DNA templates were produced using overlapping oligonucleotides in a high-fidelity PCR reaction[49]. The PCR products were first purified using the QiaQuick PCR purification kit and used as a template for in vitro transcription of the sgRNA with the MEGAshort script T7 kit (ThermoFisher, AM1354). Following in vitro transcription, RNA was purified using the MEGAclear Transcription Clean-Up Kit (ThermoFisher AM1908). All samples were analyzed by Nanodrop to determine concentration and visualized using the Qiaxcel Advanced System using the RNA QC V2.0 kit to check the quality of RNA product before storage at −80 °C. A custom Ultramer DNA oligonucleotide was purchased from Integrated DNA Technologies. Cas9 mRNA was purchased from ThermoFisher (A25640). The sgRNA was reanalyzed by Nanodrop before assembling the microinjection mixtures, which consisted of Cas9 mRNA (100 ng μl^{-1}), sgRNA (20 ng μl^{-1}, each), and the donor DNA (100 ng μl^{-1}) in a final volume of 60 µl 1× PBS (RNAse-free).

C57BL/6N female mice at 24 to 32 days old were injected with pregnant mare serum 5 IU/mouse, followed 46.5 hours later with human chorionic gonadotropin 5 IU/mouse. The females were then mated to C57BL/6J males. Fertilized oocytes were collected at 0.5 dpc for microinjection. The BCM Genetically Engineered Mouse Core service microinjected the sgRNA/Cas9/ssOligo mixture into the cytoplasm of at least 200 pronuclear stage zygotes. Injected zygotes were transferred into pseudopregnant ICR females on the afternoon of the injection, at approximately 25–32 zygotes per recipient female.

To determine if the mutagenized CLEAR site had been introduced by HDR, N0 mice were genotyped by standard PCR. Two primers approximately 100–200 bases outside the CLEAR site were designed to amplify an amplicon for direct Sanger sequencing. Sequence traces were compared to WT DNA to confirm incorporation of the modified bases.

The *Atp6v1h* germline heterozygous mouse was produced by the Baylor College of Medicine Knockout Mouse Phenotyping Program (KOMP2) (https://commonfund.nih.gov/KOMP2). Specifically, exon 3, representing a critical region of the *Atp6v1h* gene, was deleted by employing two Cas9-RGN guides, one each targeting the flanking introns to this critical region. The mice were produced as described above.

The primers for mouse genotyping are listed in Supplementary Table 3.

Bulk RNA-seq and analysis

RNA was isolated from hippocampal tissues of 4- and 9-month-old WT and Tau mice using RNeasy Mini kit from Qiagen with DNase digestion. cDNA library was generated using the QuantSeq 3′ mRNA-Seq Library Prep Kit following the manufacturer's instructions. Briefly, oligo(dT) beads were used to enrich mRNA. After chemical fragmentation, the cDNA libraries were generated using NEBNext Ultra RNA Library Prep Kit for Illumina (New England Biolabs) and were assessed using Qubit 2.0 fluorometer to calculate the concentrations and Bioanalyzer Instrument to determine insert size. cDNA library samples were then sequenced using Illumina HiSeq2000 machine with a depth of 50–55 million pairs of reads per sample (Sequencing and Microarray Facility, MD Anderson). bcl2fastq was used for demultiplexing.

Cutadapt[50] was used to remove adapters and low-quality reads. Then, remaining reads were mapped to the mm10 genome using STAR[51]. Only unique mapped reads were kept for further analysis. Gene counts were produced using featureCounts with default parameters, except for 'stranded' which was set to '0'. The DESeq2 package was used to identify DEGs with the cutoff: $\log_2$(fold change) ≥ 0.5 and FDR < 0.05 (Tau (9-month-old) versus WT (9-month-old) or Tau (4-month-old) versus WT (4-month-old)).

Gene set enrichment analyses of GO and KEGG were performed by using GSEA v.4.3.2 for all expressed genes between the Tau group and WT group. Enrichment pathways were ranked based on normalized enrichment score. GO enrichment analysis was done by using Metascape (http://metascape.org/) online tool with default parameters.

ChIP-seq analysis

We downloaded public TFEB ChIP-seq data from THP1(Monocytic) cell line[52]. After removing adapters and low-quality bases, the remaining reads were mapped to hg38 reference genome by Bowtie2 (ref. 53). Alignments were processed by SAMtools[54] to remove low-quality alignments ('-q 10'), PCR duplicates and mitochondrial reads. Reads that passed this filter were used to call peaks with MACS2 (ref. 55). For visualization, each individual library was normalized to RPKM and the track for each library was then generated by bamCoverage with built-in deeptools[56] followed by searching of conserved CLEAR motif (CACGTG) within TFEB-binding sites.

snRNA-seq and analysis

Nine-month-old WT, CL, Tau and Tau;CL mice were perfused transcardially with cold saline under anesthesia. Hippocampal tissues were dissected into 1.5 ml RNAase free Eppendorf tube, flash-frozen with liquid nitrogen and stored at −80 ℃. Single-nucleus suspensions were prepared as described[57]. Nuclei stained by Hoechst-33342 were collected using the SONY SH800 FACS sorter. For each 10x Genomics run, 100k–400k nuclei were collected. 10k nuclei for each channel were loaded to the 10x controller. snRNA-seq was performed using the 10x Genomics system with 3′ v.3.1 kits. All PCR reactions were performed using the Biorad C1000 Touch Thermal cycler with 96-Deep Well Reaction Module. Overall 13 cycles were used for cDNA amplification and 16 cycles were used for sample index PCR. As per 10x protocol, 1:10 dilutions of amplified cDNA and final libraries were evaluated on a bioanalyzer. Each library was diluted to 4 nM, and equal volumes of 18 libraries were pooled for each NovaSeq S4 sequencing run. Pools were sequenced using 100 cycle run kits and the Single Index configuration. Read 1, Index 1 (i7), and Read 2 are 28 bp, 8 bp and 91 bp, respectively. A PhiX control library was spiked in at 0.2 to 1% concentration. Libraries were sequenced on the NovaSeq 6000 Sequencing System (Illumina).

Raw reads demultiplexed by bcl2fastq were mapped to the mm10 genome using CellRanger v.6.0.1 with default parameters. Ambient RNA was removed by decountX (v.1.12.0). Quality control filtering, variable gene selection, dimensionality reduction and clustering for cells were conducted using the Seurat v.4.0.6 package. To filter low-quality cells, we removed cells for which less than 200 genes were detected or cells that contained greater than 10% of genes from the mitochondrial genome. Genes expressed in fewer than three cells were filtered out. DoubletFinder v.2.0 was used to remove Doublets. Batch effect was corrected by Harmony. Gene expression count data for all samples was normalized with 'NormalizedData' function, followed by scaling

to regress UMIs by 'ScaleData' function. Principal component analysis (PCA) and UMAP implemented in the 'RunPCA' and 'RunUMAP' functions were used to identify the deviations among cells, respectively. For subtypes differential expression markers or genes were identified by using the Wilcoxon test implemented in the 'FindMarkers' function, which was considered significant with an average fold change of at least 0.25 and *P* adjusted < 0.05.

qPCR and ChIP-qPCR

For qPCR, total RNA was extracted from cell culture using a RNeasy Mini Kit (Qiagen) and cDNA was synthesized from 500 ng total RNA using SuperScript III First-Strand Synthesis System (Invitrogen). For hippocampal brain samples, TRIzol reagent (Invitrogen) was used to extract total RNA and cDNA was synthesized from 2 µg total RNA. cDNA was diluted to 2 ng µl^{-1} and 4 µl were added to 10 µl 2× FastStart Universal SYBR Green PCR Master (Roche). Each sample was run in triplicate using iTaq Universal SYBR Green Supermix (BioRad, No. 172-5124) on a CFX384 Touch Real-Time PCR Detection System. Ct values were normalized to the housekeeping gene GAPDH, which was amplified in parallel. The 2^-ΔΔCT method was utilized to calculate relative gene expression levels. The primer sequences are shown in Supplementary Table 4.

For ChIP-qPCR, N2a cells were plated in 10% FBS DMEM and allowed to grow for 48 hours before transfection with TFEB-3XFLAG or GFP plasmids. Cells were transfected according to the manufacturer's protocol at a lipofectamine (µl):plasmid (µg) ratio of 3:1 (X-tremeGENE 9, Roche). After 48 hours, chromatin was isolated (Active Motif high-sensitivity ChIP kit) and sheared (Diagenode Bioruptor bath sonicator) using 20 cycles (30 seconds on, 30 seconds off). Chromatin immunoprecipitation was performed using a mouse anti-FLAG antibody (Sigma) or normal mouse IgG (Millipore). Immunoprecipitated DNA was amplified using qPCR primer sets shown in Supplementary Table 5. Data are reported as fold change of TFEB binding normalized to input and IgG control immunoprecipitation.

Luciferase assay

HEK293 cells or N2a cells grown in 12-well plates were cotransfected with TFEB-3XFLAG expression vector and Atp6v1h wild-type promoter or CLEAR mutant promoter firefly luciferase plasmid, together with Renilla-TK luciferase vector using X-tremeGENE 9 transfection reagent (Roche). The Atp6v1h promoters were cloned into pGL3 plasmid (Promega). The CLEAR mutant promoters were generated using site-directed mutagenesis (QuikChange II XL Site-Directed Mutagenesis Kit, Agilent). Renilla plasmid was transfected at 1/20 the amount of the other plasmids. In studying the effect of tau on Atp6v1h promoter, HEK293 cells were cotransfected with the firefly luciferase Atp6v1h promoter construct, the TauP301L-V5 plasmid and the Renilla-TK construct. After 24 hours, Pff were added to seed insoluble tau. At 48 hours, cells were lysed in passive lysis buffer (Promega). The Dual-Glo Luciferase Assay System (Promega) was used to determine firefly and Renilla luciferase activities according to the manufacturer's instructions. Measurements were performed in a white 96-well plate on a Tecan Spark 10M plate reader.

In vitro tau seeding assay

The procedure was described in detail in a previous study[16]. HEK293 cells were grown in DMEM (Life Technologies) with 10% FBS at 37 °C with 5% CO_2. Cells were cultured in a 60-mm^2 dish with 5-ml medium. At 60% confluency, cells were transfected with Tau-P301L-V5 encoding full-length human tau with P301L mutation and V5 tag (GKPIPNPLLGLDST) and TFEB-GFP at a 2:1 ratio of tau:TFEB (X-tremeGENE 9, Roche). Twenty-four hours later the media was changed and 40 µl of Pff was added to the culture along with 200 nM bafilomycin (Sigma) or an equivalent volume of DMSO. At 24–48 hours after seeding, cells were collected for analysis.

Primary mixed glia and microglia cultures and treatment

Primary glia cultures were prepared as described previously[58]. Briefly, the cerebral cortices were isolated from P3 newborn pups in ice-cold dissection medium (Hanks' balanced salt solution (HBSS) with 10 mM HEPES, 0.6% glucose and 1% (v/v) penicillin/streptomycin), with meninges removed. The tissue was then finely minced and digested in 0.125% trypsin at 37 °C for 15 min, followed by the addition of trypsin inhibitor (40 µg ml^{-1}) and DNase (250 µg ml^{-1}). Next, tissue was triturated, and resuspended in DMEM with 10% FBS. The cell suspension was centrifuged and resuspended one more time to remove tissue debris. Cells were plated on 24-well culture plates with a poly-D-lysine (PDL)-coated cover slip at a density of 50,000 cells per cm^2 and cultured in DMEM with 10% FBS at 37 °C in a humidified atmosphere of 95% air and 5% CO_2 for 7–10 days. For microglia cultures, suspended cells were plated on T-75 flasks at a density of 50,000 cells per cm^2 to generate mixed glial cultures. After the mixed glial culture reached confluency, the flasks were shaken for 2 hours at 250 r.p.m. at 37 °C. The T-75 flasks were then tapped vigorously 10–15 times on the bench top to loosen microglia growing on top of the astrocytes. The media along with floating microglia were collected from the flask and centrifuged for 5 minutes at 1,000*g*. The cell pellet from one T-75 flask was resuspended and plated in PDL-coated 24-well plates. The media was changed 24 hours later. After 48–72 hours in culture, microglia were collected for experiments.

For amino acid and serum starvation, cells were incubated in prewarmed Earls Balanced Salt Solution (EBSS) (Invitrogen) at 37 °C for 4 hours to induce autophagy. LysoSensor Green DND-189 stock solution (ThermoFisher) was diluted to the final working concentration (1 µM) in either normal cell culture medium or EBSS. The cells were stained with 1 µM LysoSensor in media for 5 min. Cells were rinsed twice with 1× PBS and incubated in culture medium for confocal microscopy. For LPS treatment, 200 ng ml^{-1} LPS (Sigma-Aldrich) was added to the microglia culture media 16 hours before an experiment. Overall lysosomal hydrolytic activity was determined with DQ-BSA dye (Invitrogen). DQ-BSA stock solutions were prepared according to the manufacturer's instructions. Cells were incubated with DQ-BSA dye (10 µg ml^{-1}) for 16 hours. Images were taken using a Confocal microscope, and the fluorescence intensities of DQ-BSA were quantified with Fiji (ImageJ).

For HIF-1α inhibitor treatment, primary microglia cultures were preincubated with 60 µM Chrysin (Abcam) for 18 hours before LPS stimulation in the presence of 60 µM Chrysin. The effect of Chrysin was validated by cotreating microglia culture with hypoxic mimetic $CoCl_2$ (100 µM; Sigma) with Chrysin for 18 hours.

Acidic Nanoparticles (NP) were prepared as described[59]. Briefly, Resomer RG 503H PLGA (Sigma-Aldrich, 719870) was used with a lactide:glycoside ratio of 50:50, to prepare a stock solution of polymer with fluorophore by dissolving 10 mg of PLGA and 0.3 mg of Nile red fluorophore (Sigma-Aldrich, 19123) in 1 ml of tetrahydrofuran (THF, Sigma-Aldrich, 401757). The working solution was made by diluting 100 µl of the stock solution into 10 ml of deionized water under sonication. PLGA-aNP solutions were used as freshly prepared for all experiments and added to culture medium for 16 hours.

Immunoblotting

For Western blot, cells, forebrain or dissected hippocampus were lysed in RIPA buffer (TBS with 1% NP-40, 1% sodium deoxycholic acid, 0.1% sodium dodecyl sulfate and protease/phosphatase inhibitor cocktails (Roche)). Lysates were sonicated six pulses at 50% duty cycle and incubated on ice for 30 minutes. Samples were then centrifuged at 20,000*g* for 20 minutes. Supernatants were collected and quantified using a Pierce BCA Protein Assay Kit (ThermoFisher). Lysates were incubated for 7 minutes at 90 °C in sample loading buffer. Fifteen microgram protein samples were loaded onto 12% SDS–PAGE gels, then transferred to nitrocellulose membranes (BioRad). Membranes were blocked in 5% nonfat milk in PBS + 0.1% Tween 20 (PBS-T). Blots were probed with primary antibody, washed with PBS-T, then probed

with the appropriate HRP-conjugated secondary antibody, followed by additional washes. The signal was developed with Pierce ECL Western Blotting Substrate (ThermoFisher). Band intensity was quantified using ImageJ software (National Institute of Health) and normalized to the loading control (β-tubulin).

Immunostaining

Primary cultures grown on coverslips were fixed in 4% paraformaldehyde for 20 minutes at room temperature after multiple washes with ice-cold PBS. Following fixation, coverslips were gently washed with PBS. Coverslips were then incubated in blocking buffer (PBS + 2% donkey serum + 0.1% Triton X-100) for 1 hour at room temperature. After blocking, coverslips were incubated with primary antibodies overnight in blocking buffer at 4 °C. Coverslips were then washed in PBS followed by incubation with secondary antibodies for 2 hours in blocking buffer at room temperature. Coverslips were then washed in PBS and mounted using DAPI containing mounting media. Cells were imaged by confocal microscopy (Leica TCS SPE).

Animals were perfused transcardially with 4% paraformaldehyde in 0.1 M PBS, pH 7.4, under ketamine (300 mg kg^{-1}) and xylazine (30 mg kg^{-1}) anesthesia. Brains were harvested, postfixed in the same fixative overnight at 4 °C, dehydrated with 30% sucrose in PBS and serially sectioned at 30 µm on a sliding microtome (Leica). For immunofluorescence, sections were permeabilized in PBS/0.1% Triton X-100 for 30 minutes and blocked with 4% normal donkey serum in PBS/0.1% Triton X-100 for 1 hour at room temperature. Sections were then incubated with primary antibodies in 2% serum in PBS/0.1% Triton X-100 overnight at 4 °C. Sections were then washed and incubated with Alexa Fluor 488- or Alexa Fluor 555-conjugated secondary antibodies (Invitrogen) for 1 hour at room temperature. After washing with PBS, sections were incubated with DAPI to stain the nucleus. Images were captured using a laser-scanning confocal microscopy (Leica) and quantified with ImageJ.

Immunofluorescence quantification

Endogenous TFEB nuclear localization was quantified by measuring TFEB fluorescent area in the nucleus and total DAPI positive area per confocal image with ImageJ. Percent nuclear localization was then calculated by dividing TFEB nucleus fluorescent area with DAPI positive area. For quantification of TFEB-GFP nuclear translocation, fluorescence intensity of TFEB-GFP in nucleus and cytoplasm per cell were measured first. TFEB nuclear localization was calculated based on the ratio of fluorescence intensity in nucleus divided by fluorescence intensity in cytoplasm for each cell. In total, 10–15 images (about 5 cells per image) per treatment were analyzed.

For calculating area fluorescence of AT8, GFAP and Iba1 antibody staining, the slide containing representative slices of the entire mouse brain was scanned on an EVOS fluorescence microscope. Area fluorescence in specific brain regions was calculated after thresholding to eliminate background and nonspecific staining using ImageJ. Area fluorescence of AT8, GFAP or Iba1 staining in the hippocampus was averaged across all consistently represented sections for each animal to signify the relative pathology or gliosis within the entire volume of the brain region analyzed.

For microglia morphology quantification, Iba1-positive microglia were imaged by confocal microscopy using a 63x oil lens to generate Z-stacks of the tissue thickness (~30 µm) with a step-size of 0.5 µm. Z-stacks were analyzed using IMARIS software, in which the filament function was used to generate filaments for individual cells in the images and microglia processes were automatically rendered based on the Iba1 signal.

Antibodies. MC1, CP13 and PHF1antibodies were generous gifts from the late Peter Davies (Albert Einstein College of Medicine). All other antibodies used for immunoblotting and staining were purchased from commercial sources described in Supplementary Table 6.

Statistics

The statistical methods used for bulk and single nuclear RNA-seq are described in their respective sections. For others, data are presented as average ± standard error of the mean (s.e.m.). No statistical methods were used to predetermine sample sizes, but our sample sizes are similar to those reported in previous publications[11,12]. The samples in all in vivo experiments (snRNA-seq and immunohistochemistry) were randomly allocated to experimental groups in an age-matched and sex-matched manner. For in vitro experiments, samples were randomized before treatments. For in vitro experiments and imaging, data were collected and analyzed blindly. snRNA-seq analysis were not performed blind to genotype to correctly identify cell clusters. No data points were excluded from the analysis. Violin plots are presented as medians and quartiles. Pairwise comparisons were analyzed using a two-tailed Student's *t*-test. Grouped comparisons were made by one-way ANOVA with Sidak's correction. Data distribution was assumed to be normal, but this was not formally tested. $P < 0.05$ was considered statistically significant. Exact *P* values are labeled on each comparison except those with $P < 0.0001$.

Reporting summary

Further information on research design is available in the Nature Portfolio Reporting Summary linked to this article.

Data availability

Bulk hippocampus RNA-seq and snRNA-seq data generated in this study have been deposited in the GEO with accession number: GSE218728. Public TFEB ChIP-seq in THP1 cell line was downloaded from NCBI with the accession number GSE217608. Any additional information on sequencing data reported in this paper is available upon request. Source data are provided with this paper.

Code availability

The scripts for snRNA-seq and bulk RNA-seq analysis were deposited at https://github.com/qicy2014/snRNA_bulkRNAseq.git.

References

48. Yoshiyama, Y. et al. Synapse loss and microglial activation precede tangles in a P301S tauopathy mouse model. *Neuron* **53**, 337–351 (2007).
49. Bassett, A. R., Tibbit, C., Ponting, C. P. & Liu, J. L. Highly efficient targeted mutagenesis of Drosophila with the CRISPR/Cas9 system. *Cell Rep.* **4**, 220–228 (2013).
50. Martin, M. Cutadapt removes adapter sequences from high-throughput sequencing reads. *EMBnet J.* **17**, 10–12 (2011).
51. Dobin, A. et al. STAR: ultrafast universal RNA-seq aligner. *Bioinformatics* **29**, 15–21 (2013).
52. Martina, J. A., Jeong, E. & Puertollano, R. p38 MAPK-dependent phosphorylation of TFEB promotes monocyte-to-macrophage differentiation. *EMBO Rep.* **24**, e55472 (2023).
53. Langmead, B. & Salzberg, S. L. Fast gapped-read alignment with Bowtie 2. *Nat. Methods* **9**, 357–359 (2012).
54. Li, H. et al. The Sequence Alignment/Map format and SAMtools. *Bioinformatics* **25**, 2078–2079 (2009).
55. Zhang, Y. et al. Model-based analysis of ChIP-Seq (MACS). *Genome Biol.* **9**, R137 (2008).
56. Ramírez, F., Dündar, F., Diehl, S., Grüning, B. A. & Manke, T. deepTools: a flexible platform for exploring deep-sequencing data. *Nucleic Acids Res.* **42**, W187–W191 (2014).
57. Li, H. et al. Fly Cell Atlas: a single-nucleus transcriptomic atlas of the adult fruit fly. *Science* **375**, eabk2432 (2022).
58. Lian, H., Roy, E. & Zheng, H. Protocol for primary microglial culture preparation. *Bio Protoc.* **6**, e1989 (2016).

59. Bourdenx, M. et al. Nanoparticles restore lysosomal acidification defects: implications for Parkinson and other lysosomal-related diseases. *Autophagy* **12**, 472–483 (2016).

Acknowledgements

We are grateful to the Baylor College of Medicine Knockout Mouse Phenotyping Program (KOMP2) and the Genetically Engineered Rodent Models Core for the creation of CL and VKO mice and Cytometry and Cell Sorting Core for FACS analysis. We thank A. Cole, B. Reeves and B. Contreras for expert technical support and members of the Zheng laboratory for stimulating discussions. H.L. is a CPRIT Scholar in Cancer Research (RR200063). This study was supported by grants from the NIH (P01 AG066606, RF1 NS093652, RF1 AG020670 and RF1 AG062257 to H.Z. and R00 AG062746 to H.L.) and CureAlz Fund (to H.Z.).

Author contributions

B.W., H.M.-S. and H.Z. conceived the project. M.S. and H.L. provided input and expertise in CL mutagenesis and snRNA-seq respectively. H.M.-S. performed bulk brain RNA-seq, created CL mice and was responsible for initial set of cell and mouse experiments. B.W. carried out follow-up molecular, cellular and biochemical analyses and worked with C.Q., T.-C.L., Y.Q. and H.L. in the snRNA-seq experiments and data analysis. S.W. assisted in mouse breeding and biochemical analysis, W.X. constructed acidic nanoparticles and Y.X. performed the seeding experiment. B.W., H.M.-S. and C.Q. prepared the figures, and B.W. and H.Z. wrote the manuscript. All authors read, edited and approved the final manuscript.

Competing interests

The authors declare no competing interests.

Additional information

Extended data is available for this paper at https://doi.org/10.1038/s41593-023-01494-2.

Supplementary information The online version contains supplementary material available at https://doi.org/10.1038/s41593-023-01494-2.

Correspondence and requests for materials should be addressed to Hui Zheng.

Peer review information *Nature Neuroscience* thanks Aimee Kao and the other, anonymous, reviewer(s) for their contribution to the peer review of this work.

https://doi.org/10.1038/s41593-023-01494-2

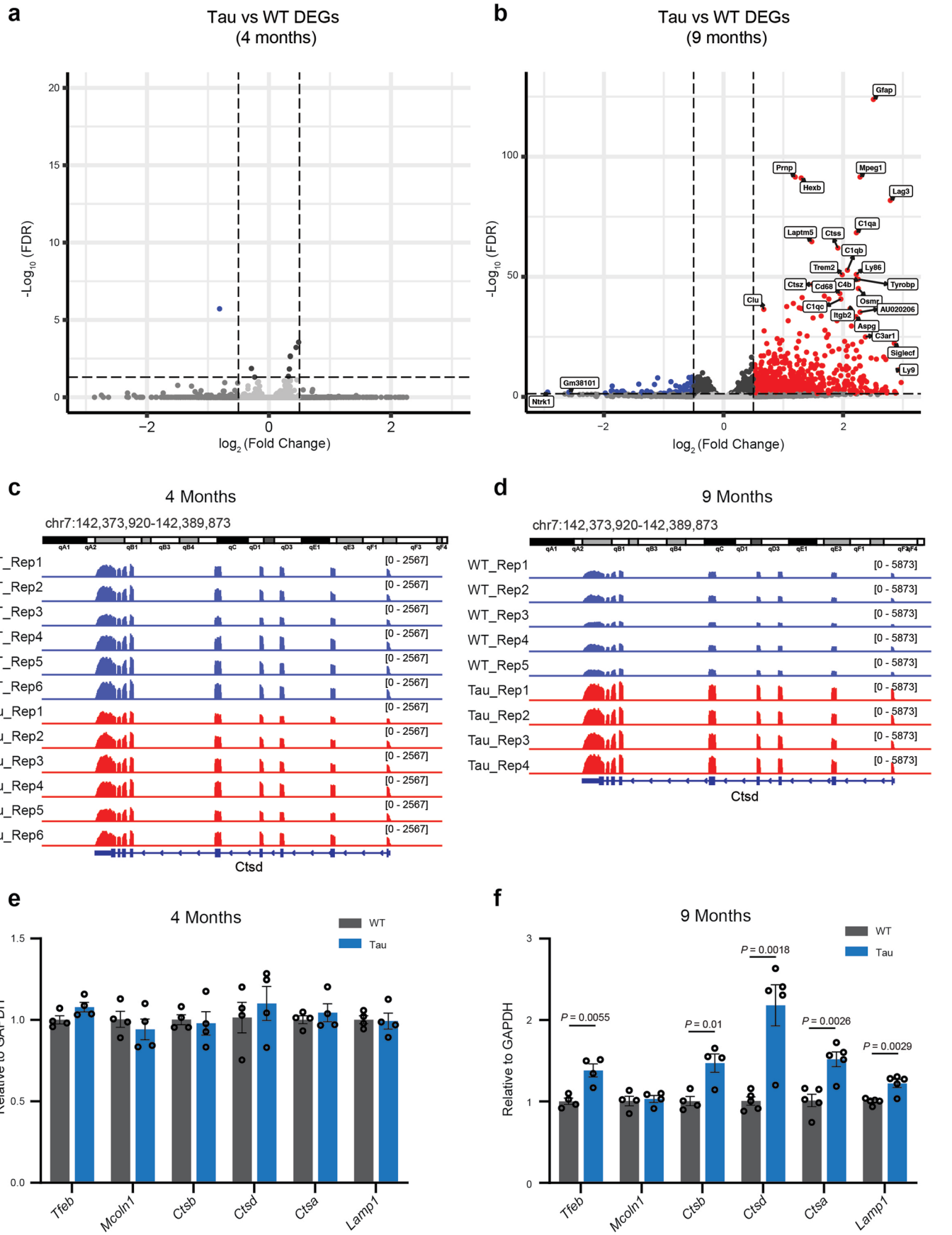

Extended Data Fig. 1 | See next page for caption.

https://doi.org/10.1038/s41593-023-01494-2

Extended Data Fig. 1 | Lysosomal and immune pathway genes are enriched in 9-month-old Tau mice. a, **b**. Volcano plots showing differentially expressed genes (DEGs) in Tau mice compared with WT mice at 4 and 9 months of age, respectively. Sample information, raw and unique mapped reads are shown in Supplementary Table 1. **c**, **d**. Snapshots of genome browser tracks of bulk brain RNA-seq of WT and Tau mice at 4 or 9 months at the *Ctsd* loci. **e**, **f**. qPCR analysis of hippocampal samples showing TFEB and TFEB regulated lysosomal genes are upregulated in 9 month-old but not 4 month-old Tau mice. Data are presented as average ± SEM. Two-tailed Student's *t*-test. N = 4 samples/group for (e). In (f), N = 4 samples/group (*Tfeb, Mucoln, Ctsb*) and N = 5 samples/group (*Ctsd, Ctsa, Lamp1*).

https://doi.org/10.1038/s41593-023-01494-2

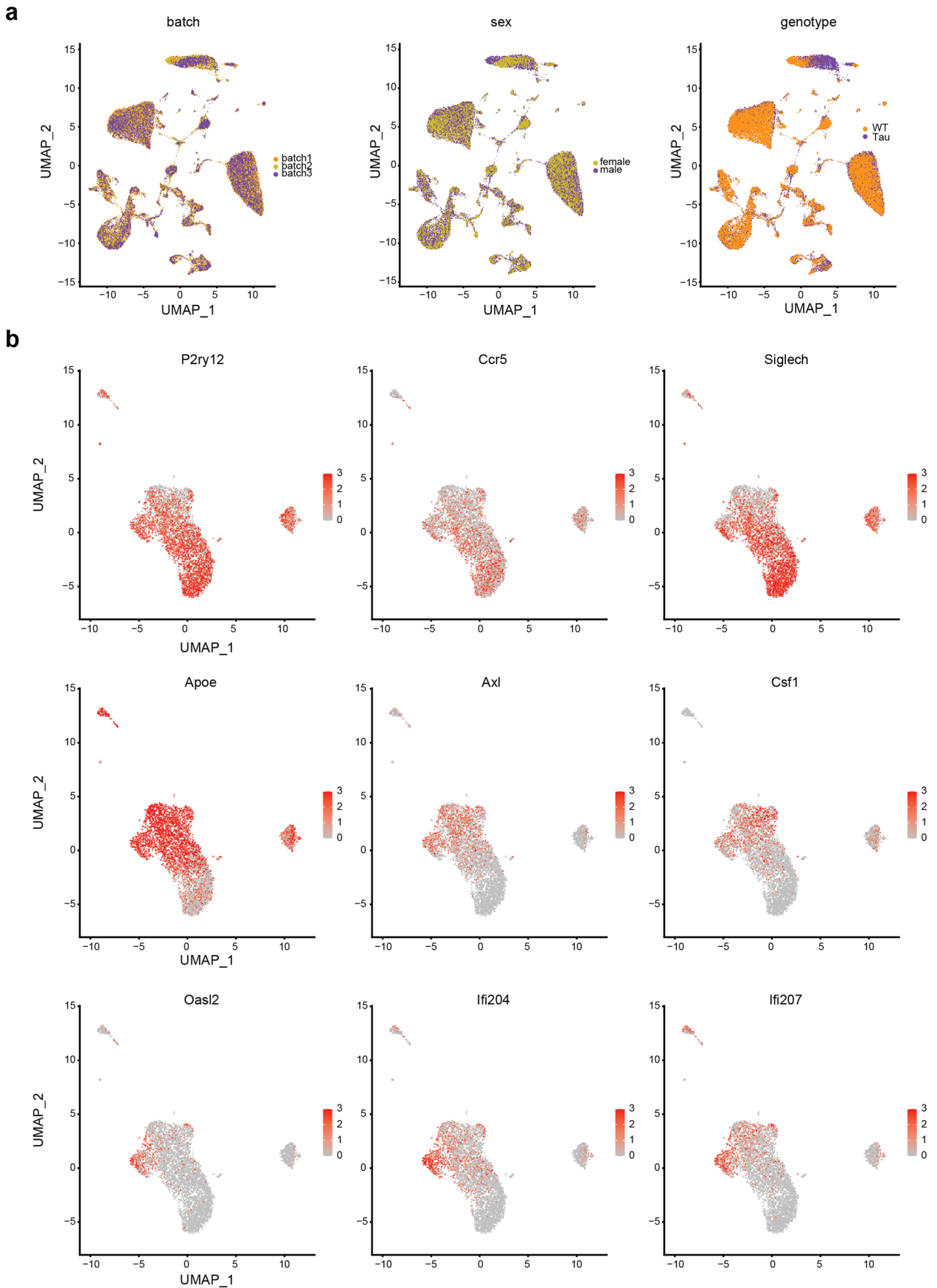

Extended Data Fig. 2 | See next page for caption.

https://doi.org/10.1038/s41593-023-01494-2

Extended Data Fig. 2 | snRNA-seq characterization of microglia subtypes. **a**. UMAP plots of 55,254 cells from hippocampus of WT and Tau mice after batch effect corrections including batch, sex and genotype. **b**. UMAP representation of reclustered microglia from WT and Tau mice analyzed by snRNA-seq. The expression levels of homeostatic microglia genes (*P2ry12, Ccr5* and *Siglech*), disease-associated-microglia genes (*Apoe, Axl* and *Csf1*) and IFN responsive-microglia genes (*Oasl2, Ifi204* and *Ifi207*) are displayed. Sample information, mean UMI per cell and cell number per library are shown in Supplementary Table 2.

https://doi.org/10.1038/s41593-023-01494-2

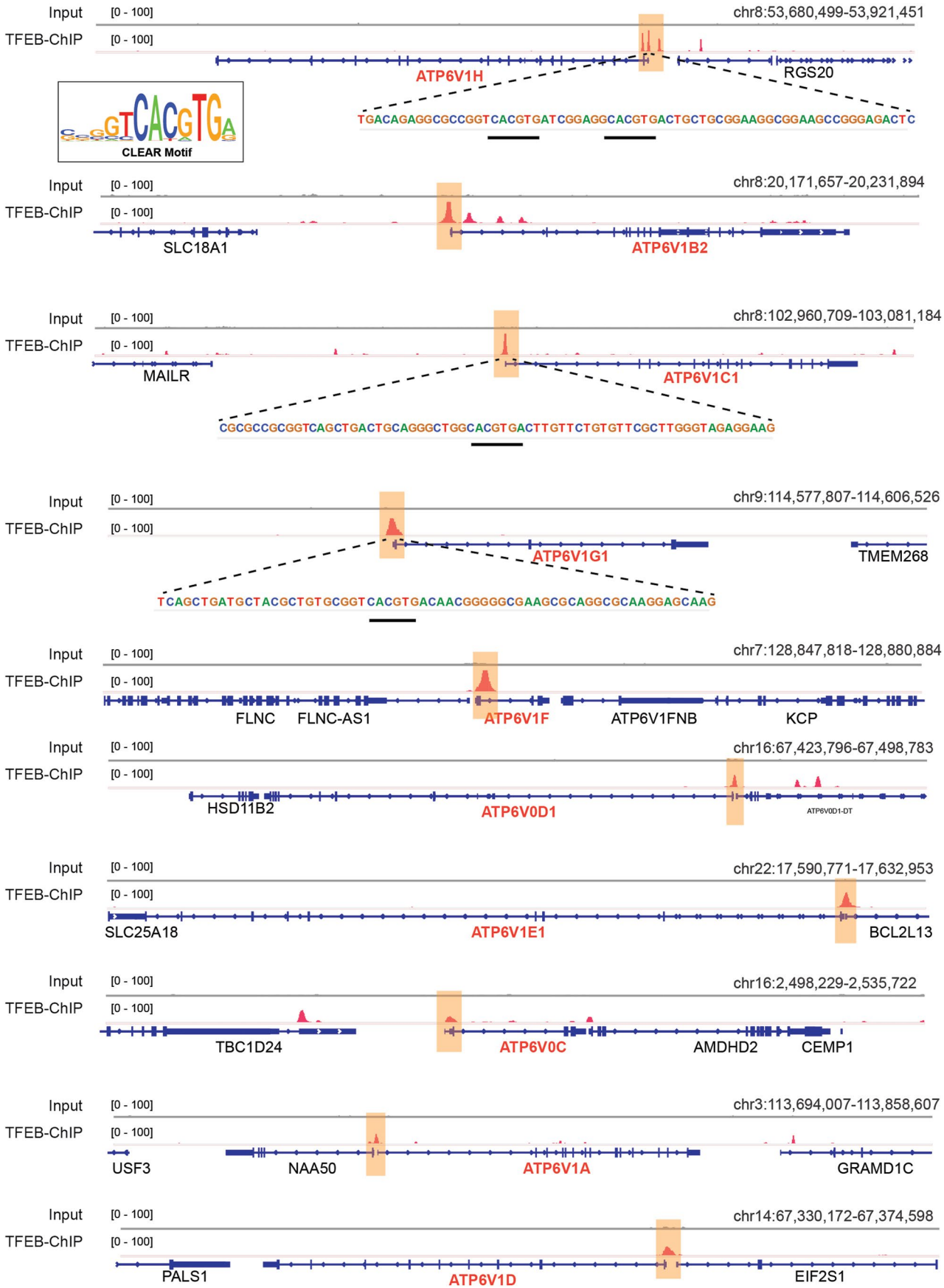

Extended Data Fig. 3 | Atp6v1h gene promoter contains strong TFEB binding sites with two tandem CLEAR sequences. Snapshots of normalized TFEB ChIP-Seq at locus of TFEB targets (ATP6V1H, ATP6V1B2, ATP6V1C1, ATP6V1G1, ATP6V1F, ATP6V0D1, ATP6V1E1, ATP6V0C, ATP6V1A, ATP6V1D). TFEB peaks are highlighted in orange box. CLEAR motifs which are zoomed-in within TFEB binding sites are marked by black lines.

https://doi.org/10.1038/s41593-023-01494-2

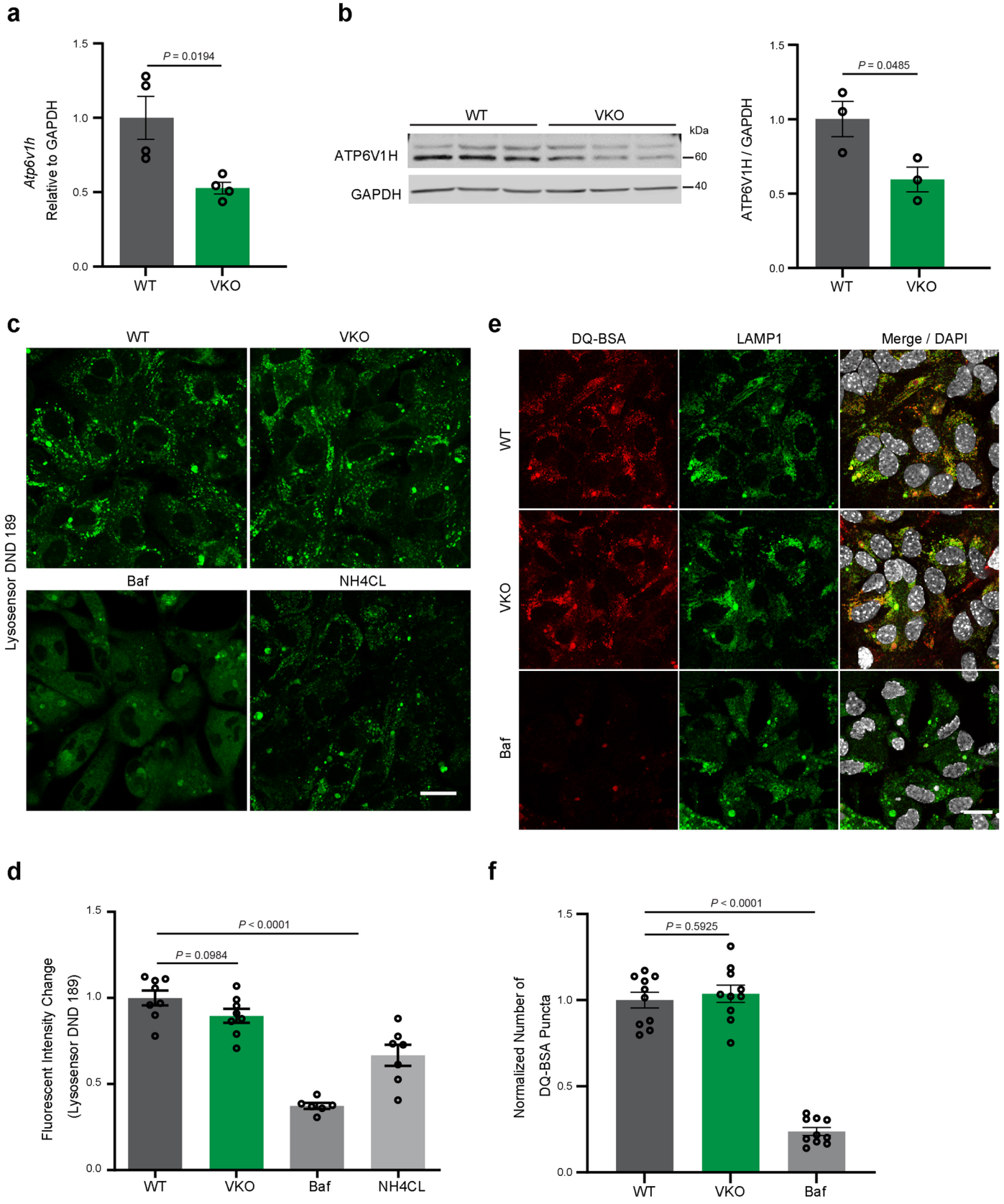

Extended Data Fig. 4 | See next page for caption.

https://doi.org/10.1038/s41593-023-01494-2

Extended Data Fig. 4 | Atp6v1h heterozygous deletion does not affect lysosomal acidification or degradative capacity. a. qPCR analysis of *Atp6v1h* transcripts in 9-month-old hippocampal tissues of WT and *Atp6v1h* heterozygous knockout (VKO). N = 4/group. **b**. Western blot with quantification of ATP6V1H protein levels in forebrain lysates of 9-month-old WT and VKO mice. N = 3/group. **c**. Representative images of LysoSensor Green DND-189 fluorescence in WT and VKO primary glial cultures. Bafilomycin (Baf) and NH4Cl treated WT cultures were used as controls. Scale bar: 10 µm. **d**. Quantification of (c) showing comparable levels of lysosomal acidification in VKO and WT cultures. N = 8 (WT; VKO); N = 6 (Baf); N = 7 (NH4CL). **e**. Representative images of DQ-BSA fluorescence co-stained with LAMP1 in WT and VKO primary glial cultures. Bafilomycin (Baf) treated WT cultures were used as a control. Scale bar: 10 µm. **f**. Quantification of (e) showing normal lysosomal degradation capacity in VKO cultures. N = 10/group. Data are presented as average ± SEM. Two-tailed t-test (a,b) and one-way ANOVA with Sidak's correction (d,f).

https://doi.org/10.1038/s41593-023-01494-2

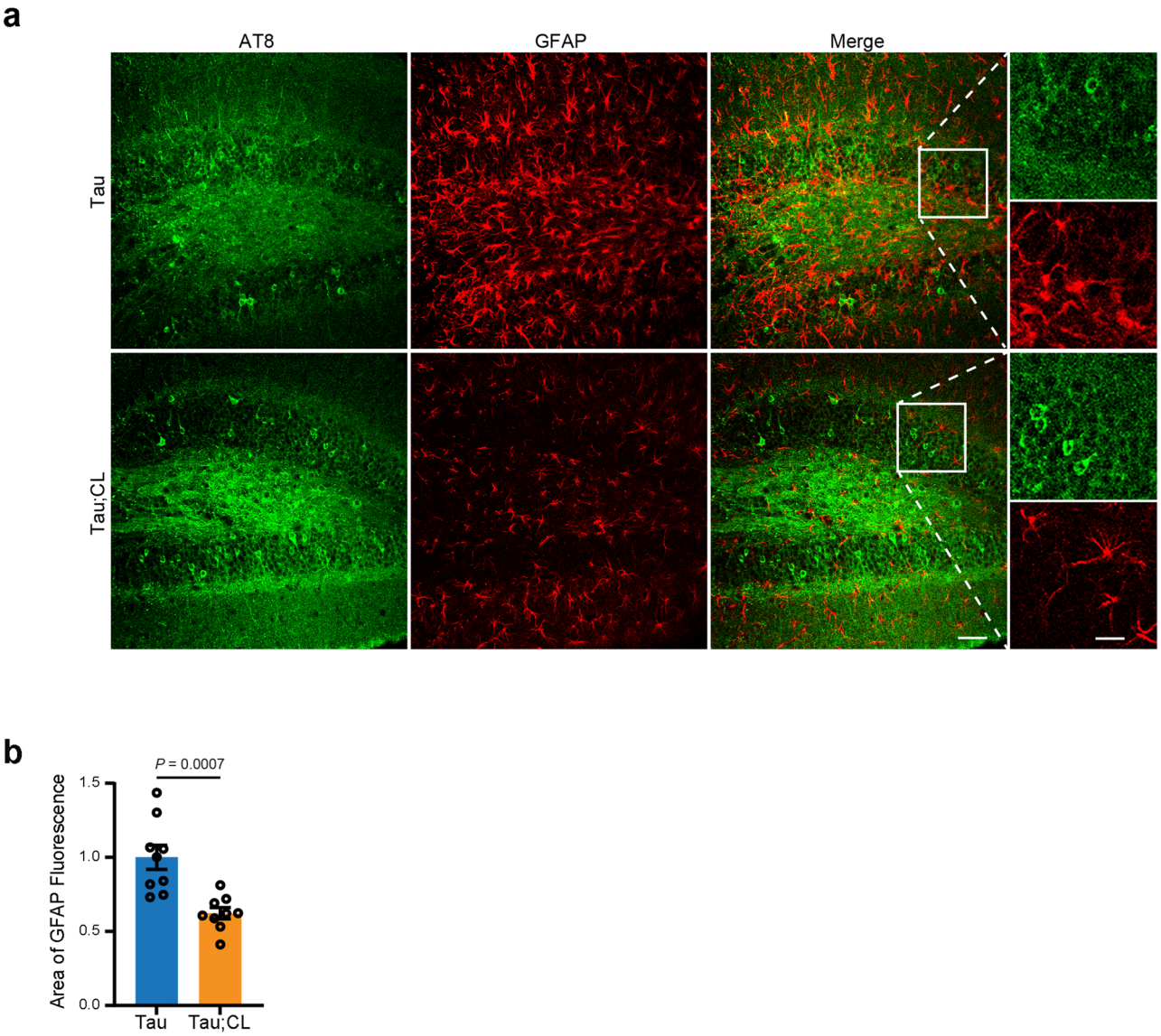

Extended Data Fig. 5 | Reduced astrogliosis in Tau;CL mice. Representative fluorescent confocal images of GFAP and AT8 immunostaining (a) with quantification (b) in the dentate gyrus of 9-month-old Tau and Tau;CL mice. Scale bar: 50 µm and 25 µm in brackets. N = 9/group. Data are presented as average ± SEM. Two-tailed Student's *t*-test.

https://doi.org/10.1038/s41593-023-01494-2

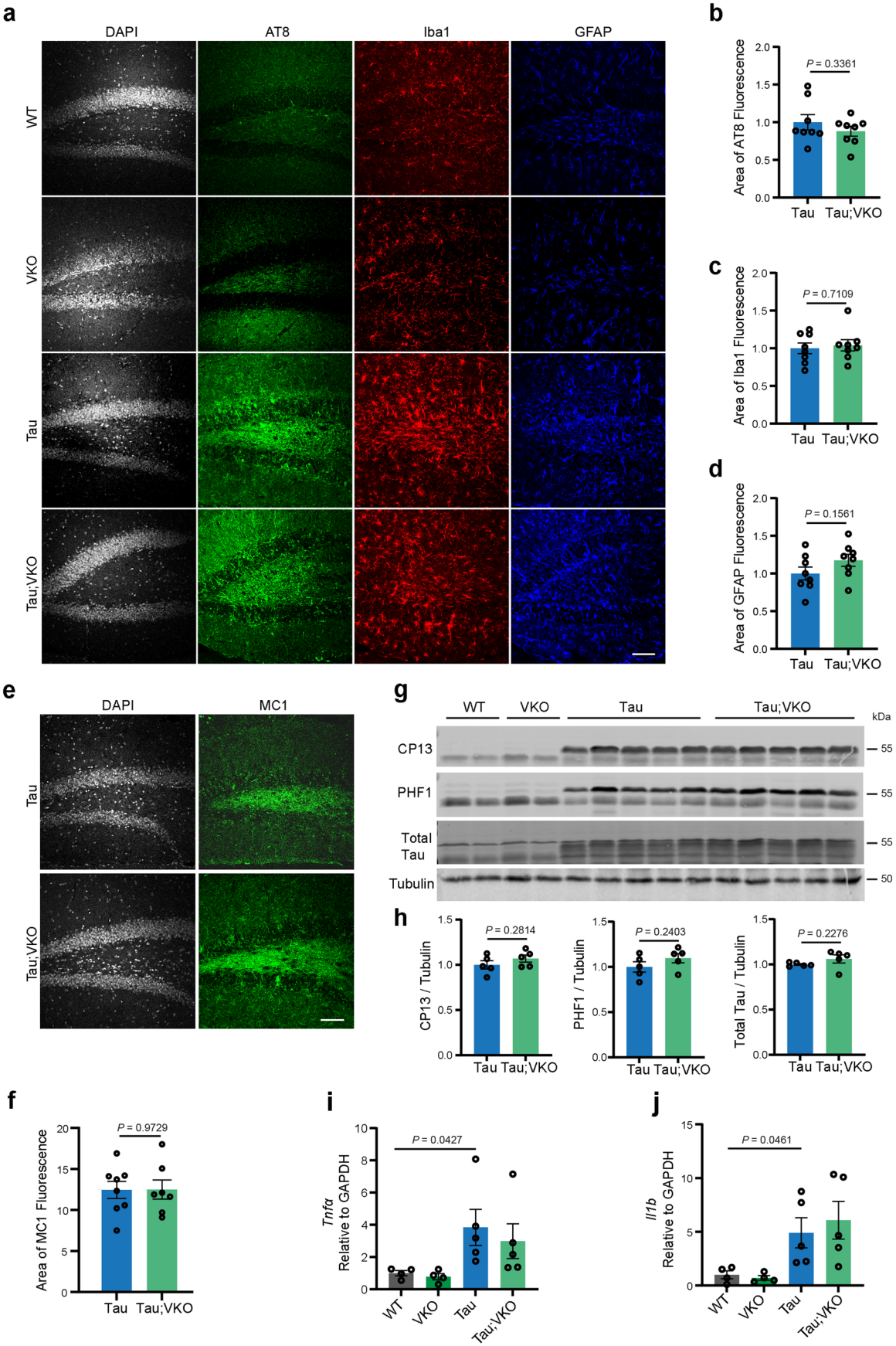

Extended Data Fig. 6 | See next page for caption.

https://doi.org/10.1038/s41593-023-01494-2

Extended Data Fig. 6 | *Atp6v1h* heterozygous deletion does not affect tau histopathology or gliosis. a. Representative fluorescent confocal images of AT8, Iba1 and GFAP in the dentate gyrus of 9-month-old WT, VKO, Tau and Tau;VKO. Scale bar: 50 µm. N = 8/group. **b**–**d**. Quantification of (a). **e**. Representative MCI fluorescent confocal images in the dentate gyrus of 9-month-old Tau and Tau; VKO mice. Scale bar: 50 µm. N = 8/group. **f**. Quantification of (e). **g, h**. Western blot (g) with quantification (h) of total and phospho-tau species recognized by CP13 and PHF1antibodies. Samples were derived from forebrain lysates of 9-month-old WT, VKO, Tau and Tau;VKO. N = 5/group. **i,j**. qPCR analysis of *Tnfa* and *Il1b* in 9-month-old WT, VKO, Tau and Tau;VKO hippocampal tissues. N = 4 (WT and VKO); N = 5 (Tau and Tau;VKO). Data are presented as average ± SEM. Two-tailed *t*-test (b,c,d,h,f) and one-way ANOVA with Sidak's correction (i,j). Tau vs. Tau;VKO: non-significant.

https://doi.org/10.1038/s41593-023-01494-2

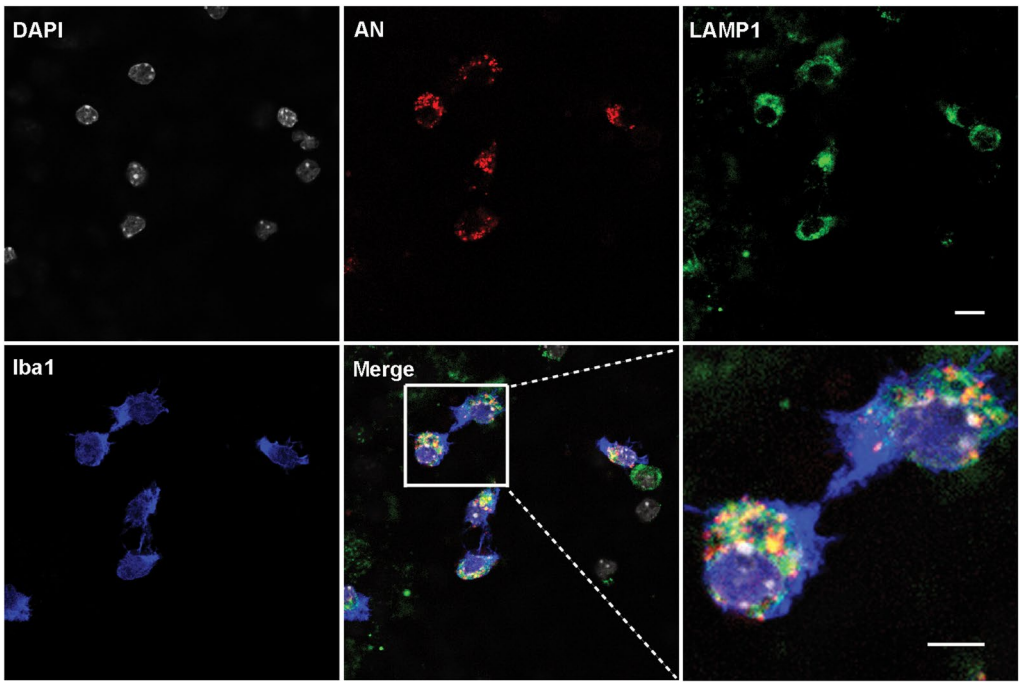

Extended Data Fig. 7 | Acidic nanoparticles are targeted to the lysosomes. Confocal images showing Acidic nanoparticles (AN) co-localized with Lamp1-marked lysosomes in microglia culture. This experiment was repeated 3 times. Scale bar: 10 µm.

https://doi.org/10.1038/s41593-023-01494-2

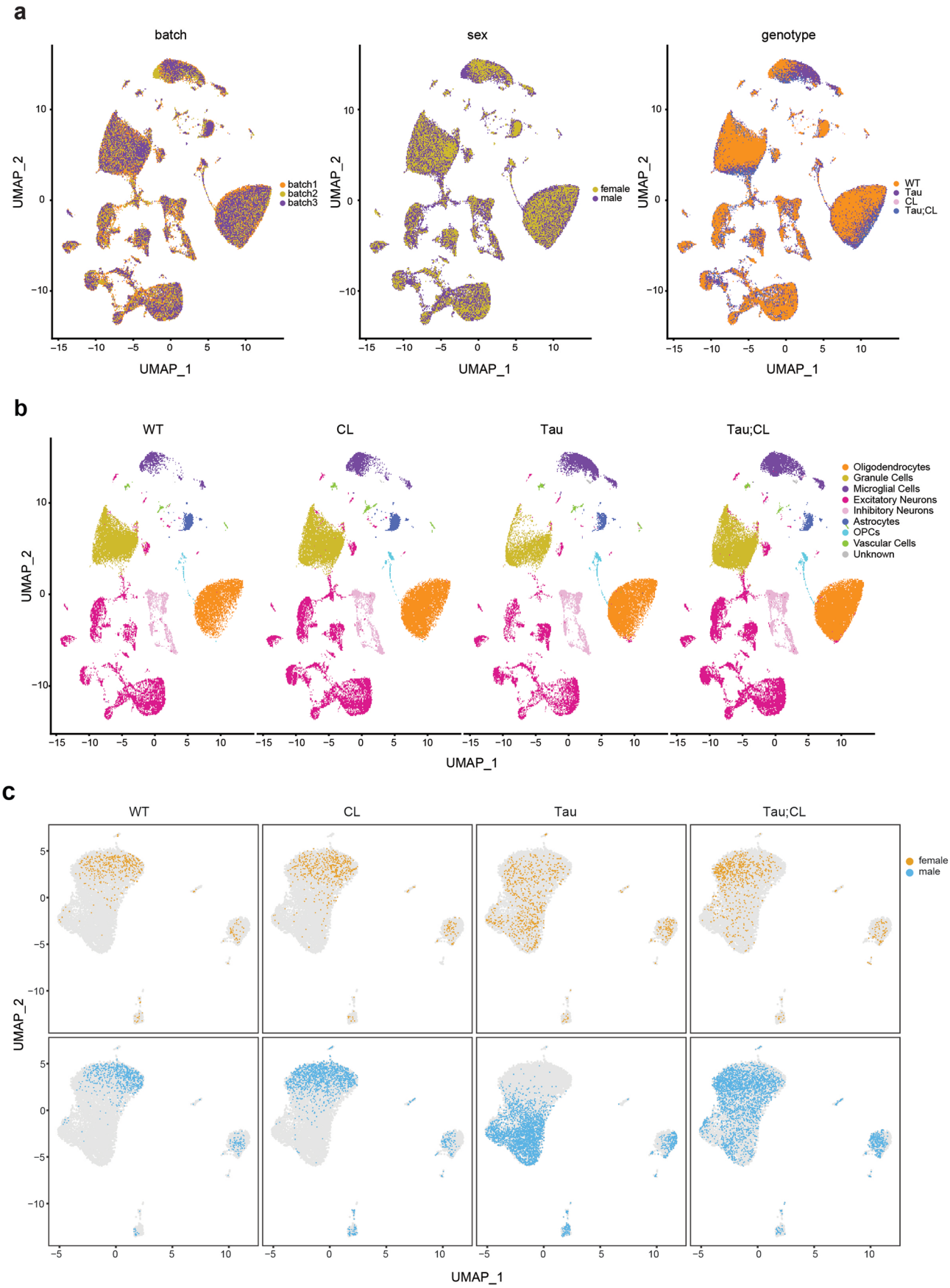

Extended Data Fig. 8 | snRNA-seq analysis of hippocampus from WT, Tau, CL and Tau;CL mice. a. UMAP plots of 137,734 cells from the hippocampus of WT, Tau, CL and Tau;CL mice after batch effect corrections including batch, sex and genotype. **b.** UMAP plots of 137,734 cells from hippocampus across each genotype. **c.** UMAP plots of re-clustered microglia cells in female (orange) and male (blue) across genotypes. Sample information, mean UMI per cell and cell number per library are shown in Supplementary Table 2.

https://doi.org/10.1038/s41593-023-01494-2

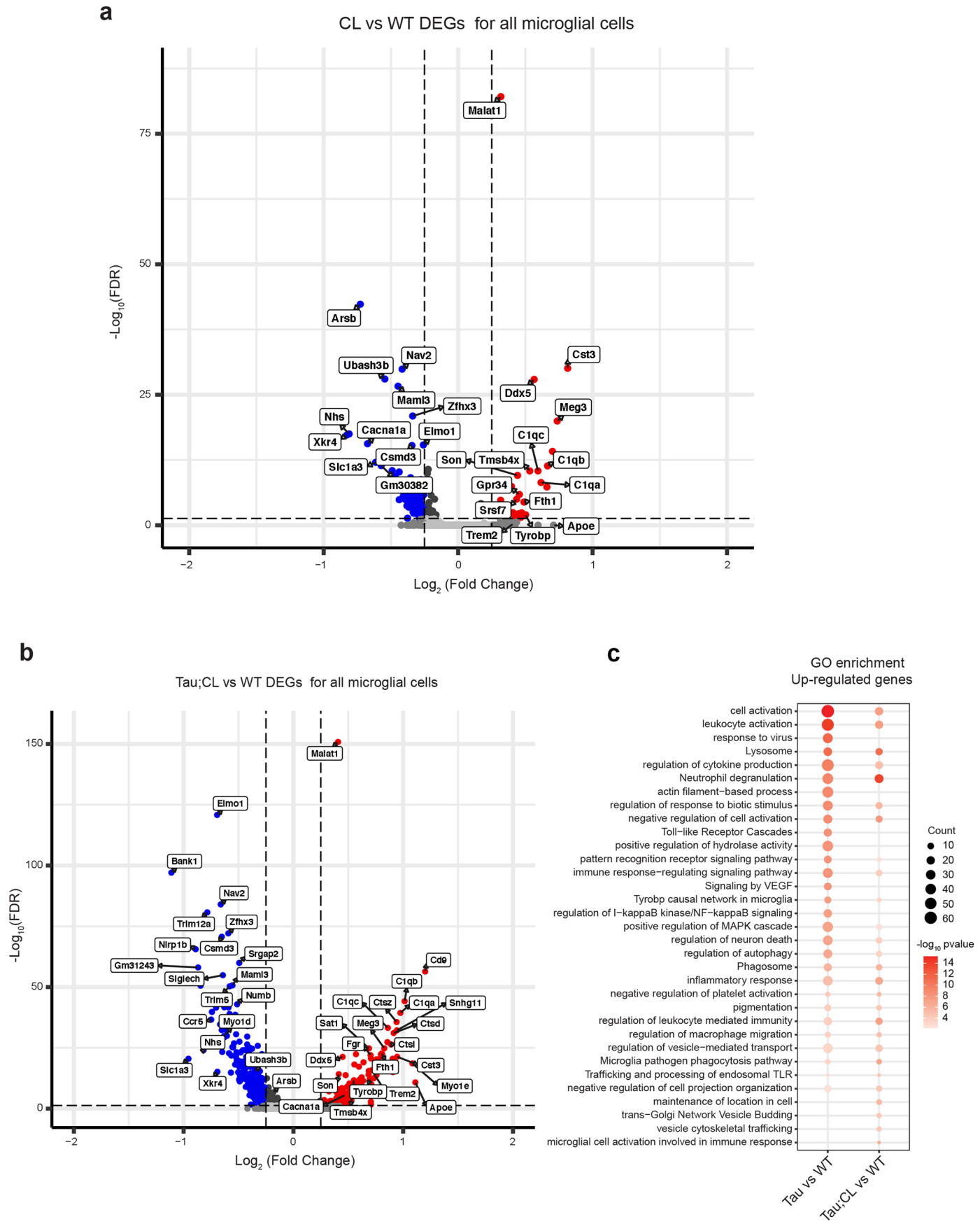

Extended Data Fig. 9 | See next page for caption.

https://doi.org/10.1038/s41593-023-01494-2

Extended Data Fig. 9 | Reduced lysosomal and inflammatory pathway genes in Tau;CL microglia. a. Differentially expressed genes analysis in CL versus WT microglia. Volcano plots showing DEGs for all microglia populations in CL versus WT mice. Up-regulated genes are highlighted in red; Down-regulated genes are highlighted in blue. **b**. Volcano plots showing DEGs for all microglia in Tau;CL versus WT genotype mice. Up-regulated genes are highlighted in red; Down-regulated genes are highlighted in blue. **c**. GO enrichment analysis for up-regulated DEGs in Tau;CL vs WT comparing with Tau vs WT. Hypergeometric test was used to identify significant enrichment pathways; FDR < 0.01.

https://doi.org/10.1038/s41593-023-01494-2

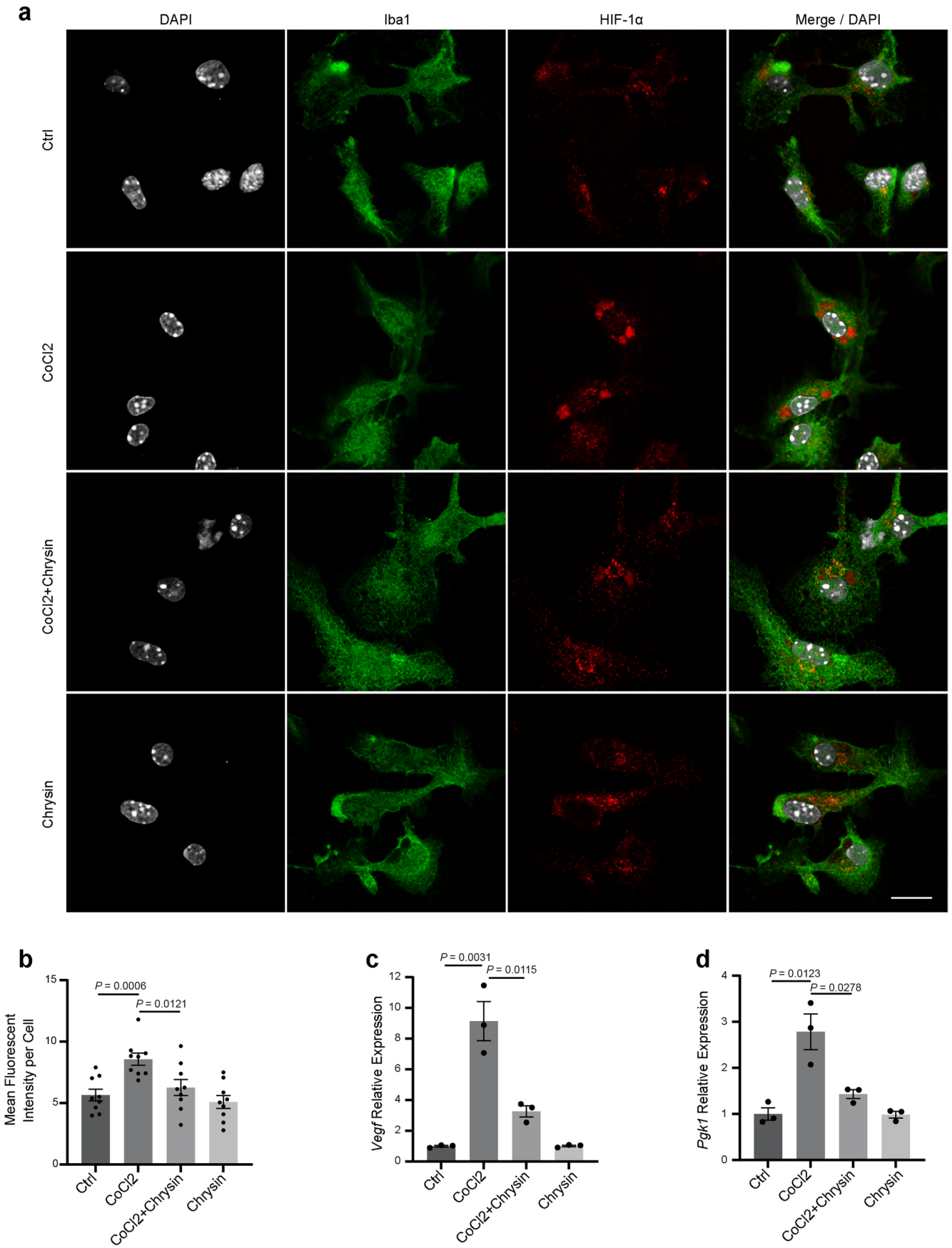

Extended Data Fig. 10 | See next page for caption.

https://doi.org/10.1038/s41593-023-01494-2

Extended Data Fig. 10 | Analysis HIF-1a inhibitor Chrysin treatment in microglia cultures. a. Representative images of HIF-1α immunofluorescence in primary microglia cultures treated with hypoxia-mimetic CoCl2 alone or co-treated with the HIF-1α inhibitor Chrysin. Scale bar: 20 µm. **b**. Quantification of (a) showing CoCl2 enhanced HIF-1α protein levels, which were abolished by Chrysin cotreatment. N = 3 independent experiments. **c**–**d**. qPCR analysis of the expression of HIF-1α downstream target genes *Vegf* and *Pgk1*. N = 3 independent experiments. Data are presented as average ± SEM. One-way ANOVA with Sidak's correction (b,c,d).

nature portfolio

Corresponding author(s): Hui Zheng

Last updated by author(s): Jun 21, 2023

Reporting Summary

Nature Portfolio wishes to improve the reproducibility of the work that we publish. This form provides structure for consistency and transparency in reporting. For further information on Nature Portfolio policies, see our Editorial Policies and the Editorial Policy Checklist.

Statistics

For all statistical analyses, confirm that the following items are present in the figure legend, table legend, main text, or Methods section.

n/a	Confirmed
☐	☒ The exact sample size (*n*) for each experimental group/condition, given as a discrete number and unit of measurement
☐	☒ A statement on whether measurements were taken from distinct samples or whether the same sample was measured repeatedly
☐	☒ The statistical test(s) used AND whether they are one- or two-sided *Only common tests should be described solely by name; describe more complex techniques in the Methods section.*
☒	☐ A description of all covariates tested
☒	☐ A description of any assumptions or corrections, such as tests of normality and adjustment for multiple comparisons
☐	☒ A full description of the statistical parameters including central tendency (e.g. means) or other basic estimates (e.g. regression coefficient) AND variation (e.g. standard deviation) or associated estimates of uncertainty (e.g. confidence intervals)
☐	☒ For null hypothesis testing, the test statistic (e.g. *F*, *t*, *r*) with confidence intervals, effect sizes, degrees of freedom and *P* value noted *Give P values as exact values whenever suitable.*
☒	☐ For Bayesian analysis, information on the choice of priors and Markov chain Monte Carlo settings
☒	☐ For hierarchical and complex designs, identification of the appropriate level for tests and full reporting of outcomes
☒	☐ Estimates of effect sizes (e.g. Cohen's *d*, Pearson's *r*), indicating how they were calculated

Our web collection on statistics for biologists contains articles on many of the points above.

Software and code

Policy information about availability of computer code

Data collection	We generated hippocampal bulk RNAseq and single nuclear RNAseq data from WT and PS19 mice using Illumina Novaseq 6000 platform. The data was demultiplexed using bcl2fastq(v1.8.4).
Data analysis	For bulk RNAseq analysis, the softwares used include: Cutadapt (v4.1), STAR (v2.5.4), samtools (v1.9) ,Featurecounts and DESeq2. for snRNAseq analysis, the softwares used include: decountX (v1.12.0), DoubletFinder (v2.0), Cellranger (v6.0.1) and Seurat (v4.0.6). Images were analyzed using Fiji (ImageJ) software 1.0 (NIH) and Imaris Software 9.8 (Bitplane) . Data representation was done using Prism 9.3.1 (GraphPad Software, Inc).

For manuscripts utilizing custom algorithms or software that are central to the research but not yet described in published literature, software must be made available to editors and reviewers. We strongly encourage code deposition in a community repository (e.g. GitHub). See the Nature Portfolio guidelines for submitting code & software for further information.

Data

Policy information about availability of data

All manuscripts must include a data availability statement. This statement should provide the following information, where applicable:

- Accession codes, unique identifiers, or web links for publicly available datasets
- A description of any restrictions on data availability
- For clinical datasets or third party data, please ensure that the statement adheres to our policy

Bulk hippocampus RNA-seq and snRNA-seq data generated in this study have been deposited in GEO with accession number: GSE218728. Public TFEB ChIP–seq in THP1 cell line was downloaded from NCBI with the accession number GSE217608.
mm10 as genome reference for mapping.
The scripts for snRNA and bulk RNAseq analysis were deposited at https://github.com/qicy2014/snRNA_bulkRNAseq.git.

Research involving human participants, their data, or biological material

Policy information about studies with human participants or human data. See also policy information about sex, gender (identity/presentation), and sexual orientation and race, ethnicity and racism.

Reporting on sex and gender	N/A
Reporting on race, ethnicity, or other socially relevant groupings	N/A
Population characteristics	N/A
Recruitment	N/A
Ethics oversight	N/A

Note that full information on the approval of the study protocol must also be provided in the manuscript.

Field-specific reporting

Please select the one below that is the best fit for your research. If you are not sure, read the appropriate sections before making your selection.

☒ Life sciences ☐ Behavioural & social sciences ☐ Ecological, evolutionary & environmental sciences

For a reference copy of the document with all sections, see nature.com/documents/nr-reporting-summary-flat.pdf

Life sciences study design

All studies must disclose on these points even when the disclosure is negative.

Sample size	No statistical methods were used to predetermine sample size. Study sizes were based on comparable experiments previously published (Ghoshet al., Sci Transl Med. 2020). For in vivo study, sample size "n" represents the number of animals used. For in vitro study, sample size "n" represents the number of independent experiments performed. For snRNAseq experiments, 4 animals (2 males + 2 females) were used per genotypes, and ~10,000 cells for each biological replicate.
Data exclusions	There were no data exclusions.
Replication	The exact number of repetitions (individual data points from each cells and/or animal) are indicated in figure legends. 3-6 independent replicate for each experiment was performed. All replication were successful.
Randomization	The samples in all in vivo experiments (snRNA-seq and immunohistochemistry) were randomly allocated into experimental groups in an age-matched and sex-matched manner. For in vitro experiments, samples were randomized before treatments.
Blinding	For in vitro experiments and imaging, data were collected and analyzed blindly. RNAseq analysis were not performed blind to genotype in order to correctly identify cell clusters.

Reporting for specific materials, systems and methods

We require information from authors about some types of materials, experimental systems and methods used in many studies. Here, indicate whether each material, system or method listed is relevant to your study. If you are not sure if a list item applies to your research, read the appropriate section before selecting a response.

Materials & experimental systems

n/a	Involved in the study
☐	☒ Antibodies
☐	☒ Eukaryotic cell lines
☒	☐ Palaeontology and archaeology
☐	☒ Animals and other organisms
☒	☐ Clinical data
☒	☐ Dual use research of concern
☒	☐ Plants

Methods

n/a	Involved in the study
☒	☐ ChIP-seq
☒	☐ Flow cytometry
☒	☐ MRI-based neuroimaging

Antibodies

Antibodies used	FLAG (Mouse, Sigma, F3165) FLAG (Rat, BioLegend, #637304)

FLAG (Rabbit, Cell Signaling Technology, #14793S)
γ-tubulin (Mouse, Sigma, T6557)
Total Tau (Rabbit, Dako, A0024)
Iba1 (Rabbit, WAKO, #019-19741)
Iba1 (Goat, Novus Biologicals, NB100-1028)
GFAP (Rabbit, Millipore, AB5804)
GFAP (Goat, Sigma, SAB2500462)TA307969
TFEB (Rabbit, Cell Signaling Technology, 4240S)
AT8 (Mouse, Thermo, MN1020)
Lamp1 (rat, BD Biosciences, #553792)
Hif1a (Rabbit, Cell Signaling Technology, #14179)
ATP6V1H (Rabbit, OriGene Technologies, #TA307969)
GAPDH (Mouse, invitrogen, #AM4300)
CD68 (Rabbit, Abcam, #125212)

Validation

Most of the antibodies used in this study are commercially available and have been validated by the manufacturers (see technical data sheets accessible on the manufacturers' websites). MC1, CP13 and PHF1antibodies were gifts from the late Peter Davies (Albert Einstein College of Medicine) and have been validated (Davies P. Methods. Mol. Med. 2000).

Eukaryotic cell lines

Policy information about cell lines and Sex and Gender in Research

Cell line source(s)	Neuro-2a (N2a) cells and HEK293 cell were from ATCC (https://www.atcc.org/products/ccl-131).
Authentication	None of the cell lines used were authenticated.
Mycoplasma contamination	Cell were routinely tested for mycoplasma and all cell lines were tested negative for mycoplasma contamination.
Commonly misidentified lines (See ICLAC register)	No commonly misidentified lines were used.

Animals and other research organisms

Policy information about studies involving animals; ARRIVE guidelines recommended for reporting animal research, and Sex and Gender in Research

Laboratory animals	Mouse lines used in this study include wild type (WT), PS19 mice (obtained from Jackson Labs; JAX:008169), CL mice (harbors CLEAR mutation in Atp6v1h promoter) and VKO mice (Atp6v1h heterozygous knockout mice). Heterozygotes are bred to B6C3F1/J wild type mice to maintain the lines. Mice were analyzed between 4 and 10 months, and the precise age used in each experiment was specified in the figure legends. Mice were with ad libitum access to food and water and were housed in mixed-genotype groups of 3–4 per cage under specific pathogen-free conditions (22 degrees celcius) with 12 h light/dark cycle.
Wild animals	This study did not involve the use of wild animals.
Reporting on sex	Both male and female mice of similar numbers were used in experiments.
Field-collected samples	This study did not involve samples collected from the field.
Ethics oversight	All protocols involving mice were approved by the Institutional Animal Care and Use Committee of Baylor College of Medicine. Protocol Number: AN-1853.

Note that full information on the approval of the study protocol must also be provided in the manuscript.